TU Delft

Delft University of Technology

Aerodynamic Interaction Effects Between Propellers in Typical eVTOL Vehicle Configurations

Stokkermans, T.C.A.; Usai, D.; Sinnige, T.; Veldhuis, L.L.M.

DOI
10.2514/1.C035814

Publication date
2021

Document Version
Final published version

Published in
Journal of Aircraft: devoted to aeronautical science and technology

Citation (APA)
Stokkermans, T. C. A., Usai, D., Sinnige, T., & Veldhuis, L. L. M. (2021). Aerodynamic Interaction Effects Between Propellers in Typical eVTOL Vehicle Configurations. *Journal of Aircraft: devoted to aeronautical science and technology*, *58*(4), 815-833. https://doi.org/10.2514/1.C035814

Important note
To cite this publication, please use the final published version (if applicable).
Please check the document version above.

Copyright
Other than for strictly personal use, it is not permitted to download, forward or distribute the text or part of it, without the consent of the author(s) and/or copyright holder(s), unless the work is under an open content license such as Creative Commons.

Takedown policy
Please contact us and provide details if you believe this document breaches copyrights.
We will remove access to the work immediately and investigate your claim.

This work is downloaded from Delft University of Technology.
For technical reasons the number of authors shown on this cover page is limited to a maximum of 10.

Green Open Access added to TU Delft Institutional Repository

'You share, we take care!' - Taverne project

https://www.openaccess.nl/en/you-share-we-take-care

Otherwise as indicated in the copyright section: the publisher is the copyright holder of this work and the author uses the Dutch legislation to make this work public.

JOURNAL OF AIRCRAFT
Vol. 58, No. 4, July–August 2021

Aerodynamic Interaction Effects Between Propellers in Typical eVTOL Vehicle Configurations

Tom C. A. Stokkermans*
Delft University of Technology, 2629 HS Delft, The Netherlands
Daniele Usai†
Politecnico di Torino, 10129 Torino, Italy
and
Tomas Sinnige‡ and Leo L. M. Veldhuis§
Delft University of Technology, 2629 HS Delft, The Netherlands

https://doi.org/10.2514/1.C035814

Many electric vertical takeoff and landing concepts are characterized by nontraditional vehicle layouts with distributed propellers. Two propeller interaction types were distinguished in this Paper, which investigates how propeller interaction in side-by-side and one-after-another configuration affects performance, in terms of thrust, power, in-plane forces, and out-of-plane moments, and how those performance effects depend on axial and lateral propeller spacing. A wind-tunnel experiment was performed with two propeller units, one instrumented with a force/torque sensor and the other introducing the aerodynamic interaction. Total pressure and planar particle-image velocimetry measurements were taken to investigate slipstream characteristics. A strong dependency of interaction effects on the geometric layout was found. For side-by-side interaction characteristic of vertical takeoff and transition, interaction effects varied from weak at small angle of attack to strong at larger angles. A drop in rear propeller thrust of up to 30% was found at constant advance ratio. Keeping thrust constant resulted in power penalties up to 13% for the two propellers combined. For one-after-another interaction, characteristic of cruise, a maximum reduction of thrust of up to 80% was observed. Thrust compensation led to power penalties up to 30% for the rear propeller alone. An extended blade element momentum model captured most interaction effects with sufficient accuracy.

Downloaded by TU DELFT on August 19, 2021 | http://arc.aiaa.org | DOI: 10.2514/1.C035814

Nomenclature

C_{F_y}	=	y-force coefficient; $F_y/(\rho_\infty n^2 D_p^4)$
C_{F_z}	=	z-force coefficient; $F_z/(\rho_\infty n^2 D_p^4)$
C_{M_y}	=	y-moment coefficient; $M_y/(\rho_\infty n^2 D_p^5)$
C_{M_z}	=	z-moment coefficient; $M_z/(\rho_\infty n^2 D_p^5)$
C_P	=	power coefficient; $P/(\rho_\infty n^3 D_p^5)$
C_p	=	pressure coefficient; $(p - p_\infty)/q_\infty$
C_{p_t}	=	total pressure coefficient; $(p_t - p_{t_\infty})/q_\infty$
C_T	=	thrust coefficient; $T/(\rho_\infty n^2 D_p^4)$
c	=	chord, m
D	=	diameter, m
d_x	=	axial distance between propellers, m
d_y	=	lateral distance between propellers, m
F	=	force, N
J	=	advance ratio; $V_\infty/(nD_p)$
M	=	moment, N · m
M_{tip}	=	helical tip Mach number based on n and V_∞
n	=	propeller rotational speed, s^{-1}
P	=	shaft power, W
P_C	=	power coefficient based on V_∞; $P/(\rho_\infty V_\infty^3 D_p^2)$
p	=	static pressure, Pa
q	=	dynamic pressure, Pa
R	=	radius, m
Re	=	Reynolds number
r	=	radial coordinate, m
T	=	thrust force (in x direction), N
T_C	=	thrust coefficient based on V_∞; $T/(\rho_\infty V_\infty^2 D_p^2)$
t	=	thickness, m
V	=	velocity, m/s
x	=	propeller axial coordinate, m
y	=	propeller lateral coordinate, m
z	=	propeller vertical coordinate, m
α	=	angle of attack, deg
β	=	blade pitch angle, deg
ρ	=	density, kg/m^3

Subscripts

a	=	axial
e	=	effective
front	=	front propeller
ISO	=	isolated configuration
i	=	induced
n	=	normal
OAA	=	one-after-another configuration
p	=	propeller
rear	=	rear propeller
SBS	=	side-by-side configuration
sl	=	slipstream
t	=	tangential
x	=	in propeller axial direction
y	=	in propeller lateral direction
z	=	in propeller vertical direction
∞	=	freestream
0	=	at static condition (V_∞ equals 0 m/s)
$0.7R_p$	=	at blade section $r/R_p = 0.7$

Received 22 November 2019; revision received 7 November 2020; accepted for publication 8 January 2021; published online 31 March 2021. Copyright © 2021 by the authors. Published by the American Institute of Aeronautics and Astronautics, Inc., with permission. All requests for copying and permission to reprint should be submitted to CCC at www.copyright.com; employ the eISSN 1533-3868 to initiate your request. See also AIAA Rights and Permissions www.aiaa.org/randp.

*Ph.D. Candidate, Flight Performance and Propulsion Section, Faculty of Aerospace Engineering; tcastokkermans@gmail.com. Member AIAA.

†M.S. Graduate, Aerospace Engineering; currently Research Assistant, Dept. of Automotive & Aeronautical Engineering, Hamburg University of Applied Sciences.

‡Assistant Professor, Flight Performance and Propulsion Section, Faculty of Aerospace Engineering. Member AIAA.

§Full Professor, Head of Flight Performance and Propulsion Section, Faculty of Aerospace Engineering. Member AIAA.

Downloaded by TU DELFT on August 19, 2021 | http://arc.aiaa.org | DOI: 10.2514/1.C035814

I. Introduction

A. Motivation

URBAN air mobility (UAM) is an emerging market that is driven by recent developments of a range of startup companies, automotive companies, mobility providers, and aerospace industry giants [12]. Most UAM concepts rely on a fleet of (hybrid-)electric vertical takeoff and landing (eVTOL) vehicles, operating as on demand taxis over a short range [3,4]. These eVTOL vehicles are characterized by nontraditional vehicle layouts with distributed propellers or rotors with low disk loading. They mainly differ from traditional aircraft by their new propulsion architectures, which are driven by electrification of propulsion [1,5,6] and the requirement of vertical takeoff and landing. According to Kasliwal et al. [7], distributed electric propulsion is the key enabler of efficiency enhancement for eVTOL vehicles because it gives the flexibility to gain benefit from aeropropulsive interaction compared to conventional layouts. These efficiency benefits are needed to reach the required range with the current or near future battery technology.

A number of eVTOL vehicle concepts with different layouts are presented by Johnson et al. [4] and Silva et al. [8] as reference vehicles for technology development. In the work of Johnson et al., the importance is stressed for research into performance issues from rotor–rotor interaction. When aircraft have two or more main rotors, rotor–rotor interaction can have significant impact on, among others, performance and noise, and this is dependent on their arrangement. Performance effects as a function of rotor or propeller arrangement are the focus of our research. Besides the impact on vehicle performance, interaction between propellers can also be a significant source of noise due to, for example, blade–vortex interaction. Although of great importance for the realization of eVTOL vehicles, this is out of the scope of our article. The work of Ref. [8] focusses on vehicles for UAM for 550 kg payload weight or up to six passengers design mission. They mention the development of a wind-tunnel test rig to study propeller interactional aerodynamics at small scale. Despite the scale effects and lack of dynamics, such a wind-tunnel test is thought to be appropriate to evaluate aerodynamic interaction phenomena. Their experimental approach is also taken in our research.

Besides the eVTOL concepts proposed in Refs. [4,8], in Ref. [6], a conceptual design study is performed for another three eVTOL concepts. Many more different concepts are thought of by the industry. Although the variety in eVTOL concepts is large, two key propeller interaction types are distinguished in this Paper that occur on many of them. The Aurora Passenger Air Vehicle [9] and the Airbus Vahana [10] are taken as examples, and their propulsion layout is sketched in Figs. 1a and 1b, respectively. For the concept from Aurora, eight propellers are used for lift at vertical takeoff and during transition to forward flight. These propellers are placed side by side (SBS) with the propeller disks in the same plane. They experience a zero propeller angle of attack α_p inflow at vertical takeoff. The close proximity of the propellers and their slipstreams, in case of a small lateral distance d_y, may affect propeller performance. The vertical takeoff is followed by a transition phase where α_p changes from 0 to approximately 90 deg. Concepts where a wing is used for lift often do not deploy such propellers for lift in forward flight, but for multicopter eVTOL concepts, a third flight condition to consider for propeller interaction is forward flight at angles around $\alpha_p = 90$ deg. Of particular interest in this Paper are propellers positioned in a line in the flight direction like in the sketched concept and not next to each other in the spanwise direction. In transition and forward flight, one can expect an interaction of the slipstream of the front propeller with the slipstream of the rear propeller, or even direct impingement of the slipstream from the front propeller on the rear propeller. Among others, the quadrotor concept and Lift+Cruise eVTOL aircraft presented by Silva et al. [8] are relevant side-by-side interaction cases. The Side-by-Side urban air taxi concept as presented by Ventura Diaz et al. [11] is, however, not covered in terms of propeller interaction despite its name, as the two rotors are distributed in the spanwise direction.

The second key propeller interaction type, sketched in Fig. 1b, is where propellers are placed one after another (OAA) with the propeller disks not in the same plane. Using tilt wings and multiple rotors, the Airbus Vahana [10] hovers like a helicopter, then transitions and cruises like an airplane. On this vehicle, during cruise or the last stage of transition, the rear propeller may ingest partly or fully the slipstream of the front propeller. In the Reynolds-averaged Navier–Stokes (RANS) computational fluid dynamics (CFD) simulation results shown in Ref. [10], this propeller interaction is visible between the front and rear propellers during transition. The Joby S2 concept [12] is another example where one-after-another propeller interaction may occur in certain flight conditions between propellers mounted on the wing and on the tail surfaces. A similar interaction, but at much smaller axial distance d_x, also occurs for multicopter concepts during vertical takeoff if the propellers are partially overlapping, or for propellers mounted with overlap or staggered on, for instance, the wing like for the high-lift propellers of the X-57 Maxwell [13].

B. Literature Review

Relevant previous research exists to determine propeller performance effects for eVTOL vehicles. First of all, propellers on such vehicles, especially for side-by-side configurations, experience a larger range of angle of attack than on conventional airplanes. A good understanding of angle of attack effects on isolated propeller performance is required to study such propellers when they are in interaction with other propellers. Propellers at very large angle of attack have been studied by, for example, Refs. [14–16].

In terms of aerodynamic interaction effects, depending on the layout of the propellers on the eVTOL vehicle, already a lot can be learned from previous research on tandem-rotor helicopters, tilt rotors, tilt wings, and multicopter concepts. However, results from tandem rotors are not necessarily applicable to propellers as they feature articulated, high-aspect ratio blades with no or low twist, while the studied rigidly mounted propeller blades have high twist and are of lower aspect ratio.

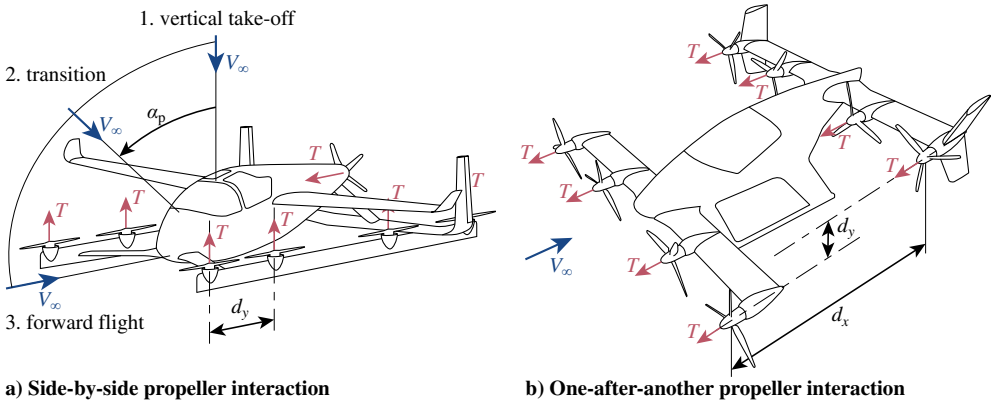

a) Side-by-side propeller interaction b) One-after-another propeller interaction

Fig. 1 Sketches of SBS and OAA propeller configurations on eVTOL vehicles based on the Aurora Passenger Air Vehicle [9] and Airbus Vahana [10], respectively.

Downloaded by TU DELFT on August 19, 2021 | http://arc.aiaa.org | DOI: 10.2514/1.C035814

A large part of the literature treats aerodynamic interaction between rotors in the hover condition, for example, Refs. [17–21].

For a tandem rotor in forward flight, Heyson [22] established experimental flowfield interaction results, reporting downwash angles and visualizing the flowfield with a five-hole probe survey. These results are relevant for side-by-side interaction at $\alpha_p = 90$ deg. Performance results of this experiment were reported by Dingeldein [23]. In forward flight, the rear rotor, located at $d_y/R_p = 2.06$ behind the front rotor, is seen to operate in a region of increased downwash of the front rotor, increasing its power requirement to maintain the same thrust compared to the same rotor in an isolated configuration. The front rotor operates in the upwash from the rear rotor, reducing the effective downwash for the front rotor and increasing its thrust for unchanged operating conditions. According to Dingeldein, the front rotor could be modeled with fair agreement using isolated rotor theory in the freestream and the rear rotor using isolated rotor theory when modeled in the fully developed downwash of the front rotor.

Stepniewski and Keys [24] describe how for tandem rotors in forward flight the rear rotor operates in the wake of the front rotor and experiences a flow with higher axial velocity component than the isolated rotor, resulting in a higher induced power. It is shown how the distance of the rear rotor to the front rotor wake influences the rear rotor performance, and a maximum induced power is found when the front rotor wake passes through the rear rotor. This power penalty reduces when the wake passes above or below the rear rotor. The largest penalty for a hypothetical tandem rotor results in a 23% increase in shaft power and occurs at the airspeed of minimum power and decreases at lower or higher speeds. Lee et al. [25] also present performance predictions of (overlapping) tandem rotors in forward flight with a free-wake panel method.

A very relevant case of rotor interaction is found on the Bell Boeing Quad tilt rotor [26] which, depending on the flight condition, experiences side-by-side interaction at various angles of attack or one-after-another interaction for an axial distance of $d_x/R_p \approx 2$. Transition and forward flight were studied with RANS CFD simulations. Just like for the tandem rotor, the rear rotor is affected by downwash of the front rotor in a side-by-side interaction, resulting in a slight reduction of thrust of the rear rotor during transition. Also, changes in rear rotor loading in forward flight are reported when the rotors are in a one-after-another configuration, especially in the region where the hub vortex of the front rotor impinges on the rear rotor. In this region, the maximum in rear rotor thrust was found as a result of the high tangential velocity and low axial velocity component in the flow.

Relevant research on propeller interaction has also been performed on much smaller scale for unmanned aerial vehicle (UAV) applications. The small propellers used for these applications are often quite flexible and operate at a low rotational speed for their size, resulting in aerodynamic twist and relatively low blade section Reynolds numbers compared to full-scale propellers on eVTOL vehicles. Despite these drawbacks, the interaction phenomena at small scale and full scale may be similar. A considerable amount of research has been done on the performance of overlapping rotors for UAVs in hover condition, for example, Refs. [27–30]. These studies, relevant for one-after-another interaction, all conclude that, compared to isolated propellers with increasing overlap, either the power demand of the rear rotor for equal thrust increases or the thrust reduces for equal power.

The performance effects of propeller interaction in side-by-side configuration have also been studied for UAV applications, mainly again in hover condition in, for example, Ref. [31]. Alvarez and Ning [32] simulated the experiment from Ref. [31] using a viscous vortex particle method. For three Reynolds numbers in forward flight, a range of advance ratios were simulated for $\alpha_p = 0$ deg. It was found that, when propellers are in close proximity, propeller interaction is detrimental for the propulsive efficiency, resulting in a maximum efficiency drop of almost 3%. This drop in performance was more accentuated at low advance ratios.

The only UAV results in forward flight with $\alpha_p = 90$ deg are presented by Ventura Diaz and Yoon [33], showing detached-eddy simulation results of a quadcopter UAV with side-by-side interaction. They found that in forward flight the propeller interaction is stronger than in hover because the wakes of the front propellers interfere with the rear propellers. They experimented successfully with different mounting to get the propellers out of same plane in order to reduce interaction effects.

C. Objective and Approach

Although there is already a large body of knowledge on aerodynamic interaction effects between propellers, it is often limited to a hover condition, and especially studies of transition and forward flight are lacking. Furthermore, there is a lack of studies with nonarticulated rotors with well-defined geometry. In general, a reference dataset with effects of interaction on in-plane forces and out-of-plane moments also does not exist. Therefore, the objective of this Paper is to investigate how propeller interaction in side-by-side and one-after-another propeller configuration affects propeller performance, in terms of thrust, power, in-plane forces, and out-of-plane moments, and how those performance effects depend on propeller spacing defined by d_x and d_y.

An experimental approach was chosen over a numerical approach, as many different configurations could be studied within a limited amount of time and no modeling errors are introduced. A drawback of the experimental approach is that, because the experiment is not at the same scale as real eVTOL vehicles, scale effects are present in the results. The interaction effects found at the smaller scale are, however, thought to be representative for the effects at larger scale, in agreement with Silva et al. [8]. Furthermore, wind-tunnel wall corrections need to be considered and are addressed in Sec. II.C. This experimental dataset not only reveals interaction effects but can also serve as reference dataset for validation of lower-order tools to predict propeller interaction like the free-wake model of Bagai and Leishman [34], the free-wake panel method of Lee et al. [25], the viscous vortex particle method of Alvarez and Ning [32], and other modeling methods. The investigation presented in this Paper partially includes the Master's thesis work by Usai [35]. The extended blade element momentum model results from this study are added for comparison to this research for the one-after-another configuration, to show that such a method can be used to predict performance effects for this configuration.

II. Experimental Setup

A. Wind-Tunnel Facility

The experiments were performed in Delft University of Technology's Open Jet Facility. This open-jet closed-circuit wind tunnel features a maximum freestream velocity of about 30 m/s from the octagonal outlet of 2.85×2.85 m. The settling chamber is equipped with a honeycomb flow rectifier and five screens to remove spatial velocity deviations and to reduce the turbulence level of the flow. This results in velocity deviations below 0.5% in the vertical plane at 2 m downstream of the outlet and a longitudinal turbulence intensity level below 0.24%. The contraction and outlet of the tunnel can be seen in Fig. 2a. A height-adjustable support table with a turntable enabled the correct positioning and orientation of the propeller units.

B. Propeller Units

For this experiment, two custom propeller units were designed and manufactured. Two four-bladed propellers were chosen with a radius of $R_p = 0.1524$ m, previously used by Veldhuis et al. [36] in four- and eight-bladed variants, and defined by the Fokker Aircraft Company in their internal F29 project. This propeller has also been used by Refs. [37,38] in an eight-bladed variant. The propeller blade geometry is defined in Fig. 3 in terms of radial distributions of chord, thickness, blade pitch, and airfoils. Supplemental Data S1 provides a complete description of the blade design including airfoil sections.

Each propeller was driven by an electric motor that was mounted inside an aluminum nacelle. One of the propeller units (propeller unit A) was instrumented with a static six-component force/torque (F/T) sensor for performance measurements, while the other unit (propeller unit B) was not instrumented with a F/T sensor. An exploded view of propeller unit A (with F/T sensor) is shown in Fig. 4. To measure the aerodynamic loading on the propeller blades, hub, and spinner, the electric motor was mounted to the F/T sensor. The F/T sensor was

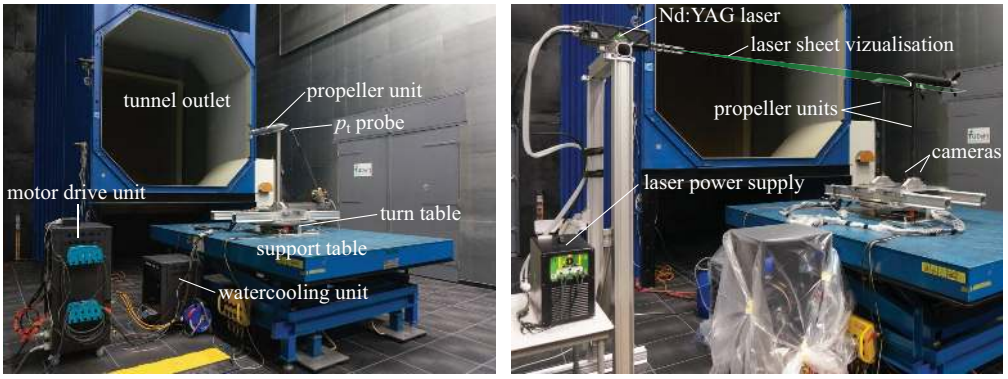

a) Setup overview with ISO propeller configuration **b) PIV setup with SBS propeller configuration**

Fig. 2 Experimental setup in Open Jet Facility at Delft University of Technology.

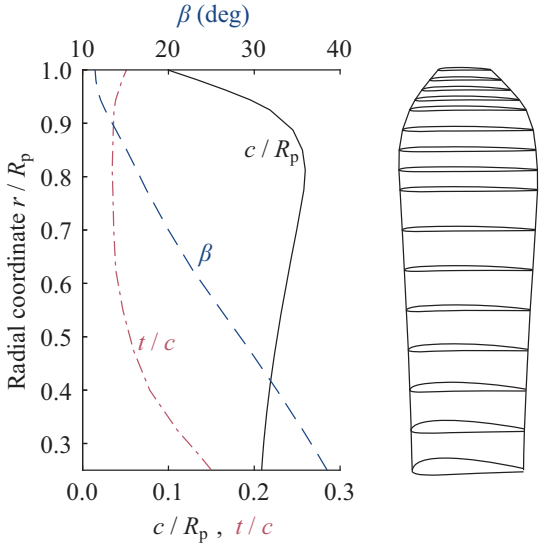

Fig. 3 Propeller blade description for $\beta_{0.7R_p} = 20.0$ deg with untwisted blade geometry and airfoils.

fixed to the nacelle via the nacelle-sensor interface (Fig. 4). The motor shaft passed through a hole in the center of the F/T sensor. On the front of the nacelle, an optical rotary encoder was mounted to measure rotational speed. To keep the temperature of the electric motor low and to prevent too large variations in F/T sensor temperature, a copper water-cooling coil was wound around the electric motor. Each electric motor was driven by an electronic speed controller connected to a 5 kW dc power supply. Both were controlled via custom control software, programmed to maintain a desired rotational speed. Maximum peak-to-peak fluctuations in rotational speed of typically 0.3% were found during the measurements. The dimensions of the propeller unit are given in Fig. 5a.

The propeller units were tested in three different configurations: as isolated (ISO) propeller, in OAA, and in SBS configuration, as sketched in Figs. 5a–5c, respectively. For the SBS configuration, as shown in Fig. 6a, both propeller units were in tractor configuration, clamped next to each other on sliding platforms attached to two beams on a turntable, to allow for change of both d_y and α_p. For the OAA configuration, as shown in Fig. 6b, the front propeller unit was placed in a pusher configuration to avoid any disturbing elements between the two propellers. In this way, the pylon of the front propeller was farthest away from the rear propeller. To convert the propeller unit from tractor to pusher configuration, the unit was turned 180 deg, the spinner was interchanged with the nacelle aftbody, and the propeller blade pitch was changed by 180 deg. Because the rotation direction of the motor was switched, the propeller rotated in the same direction in the tractor and pusher configuration. A NACA 65-021 fairing was placed over the steel pylon to reduce the wake impinging on the propeller in pusher configuration; see Fig. 4. This profile was chosen to align the profile maximum thickness with the pylon, while the profile leading edge reached up to the front of the nacelle. The change of d_y was achieved by clamping the sliding platform of the rear propeller at different locations on the beams on the support table, and d_x was varied by mounting of the rear propeller unit including

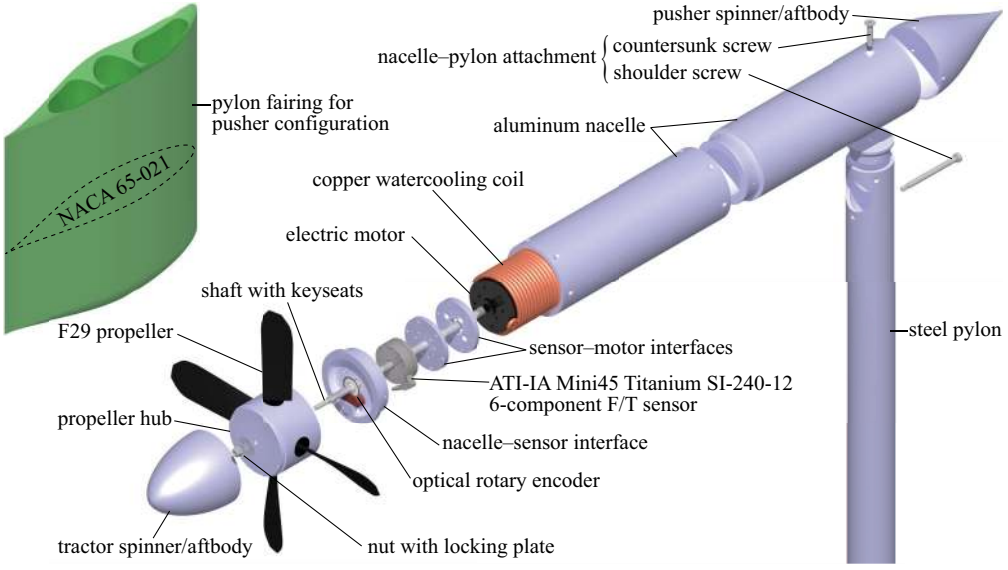

Fig. 4 Exploded view of propeller unit A with F/T sensor, indicating the various components.

Downloaded by TU DELFT on August 19, 2021 | http://arc.aiaa.org | DOI: 10.2514/1.C035814

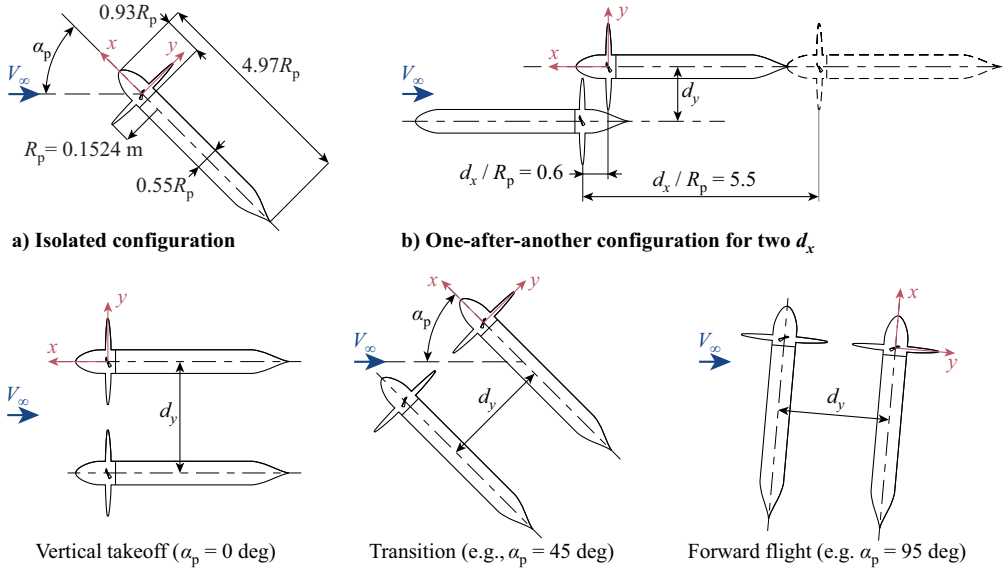

a) Isolated configuration **b) One-after-another configuration for two d_x**

c) Side-by-side configuration for the three flight phases

Fig. 5 Top view sketch of the ISO, OAA, and SBS propeller configurations, including dimensions of the tractor propeller unit.

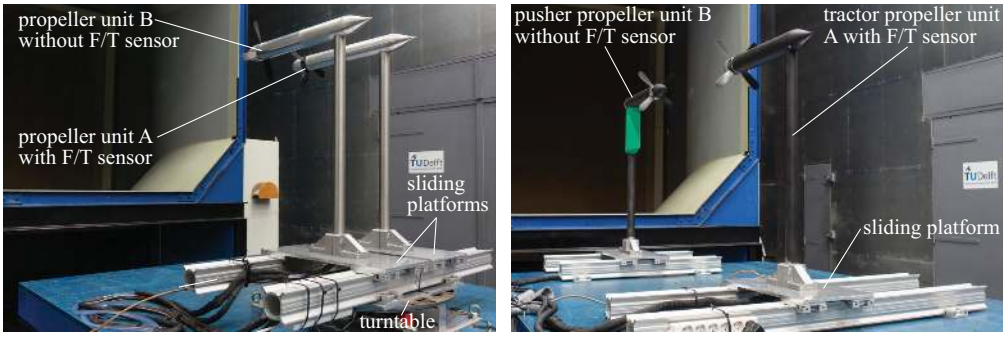

a) Side-by-side propeller configuration **b) One-after-another propeller configuration**

Fig. 6 Experimental setup of the SBS and OAA propeller configurations.

beams at a different location on the support table. CAD models of the propeller units in the tractor and pusher configuration (without pylon and fairing) are attached to the Paper as Supplemental Data S2.

C. Measurement Techniques

The sensor used to measure propeller performance was an ATI-IA Mini45 Titanium 6-component F/T sensor with SI-240-12 calibration. Variants of this sensor have also been used for propeller performance measurements in Refs. [39–44]. This sensor has a range of ±480 N for the thrust, ±240 N for the in-plane forces, and ±12 N · m for all moments. The typical effective resolution and factory tested full-scale error, established by taking the average error of a series of different calibration load cases, are 1/15 N and 0.06% for the thrust, 7/60 N and 0.23% for the in-plane forces, 1/8000 N · m and 0.04% for the torque, and 3/2000 N · m and 0.15% for the out-of-plane moments. The F/T sensor was attached to two 24 bit data acquisition cards with custom Labview data acquisition software and data were gathered at each measurement point for 10 s with 10,000 Hz sampling frequency. In line with the findings of Ref. [40], the sensor was found to be prone to drifts, especially in the thrust direction. This was mostly a result of temperature changes caused by the electric motor during testing. To minimize the effect of drifts on the results, short rotational speed sweeps were taken with a maximum of nine measurement points, and a zero measurement was taken before and after each sweep. The zero measurements were applied to the data using a linear fit based on the zeros and the measurement timestamps. Four nonconsecutive sweeps, two up and two downsweeps, were performed for each condition, and 95% simultaneous confidence bands were calculated based on those four measurements per condition. Confidence intervals based on these bands are plotted in the performance results throughout the Paper. In the work by Gunasekaran et al. [40], also a systematic error is discussed, which seems related to off-axis loading of the sensor. Considering that our setup can be categorized as an axial mount according to their definition, no such error should arise for our setup. A small reference frame transformation in the axial direction was applied to obtain the propeller performance results from the sensor reference center to the propeller center.

The presented propeller performance includes the loading on the blades, hub, and spinner as defined in Fig. 4; in other words, no blades off aerodynamic tares have been subtracted from the results. This choice was motivated partly from the observations of Ortun et al. [45] for an isolated propeller at angle of attack, which showed that the aerodynamic loading on the propeller blades cannot be separated experimentally from the loading on the spinner, except if both elements are instrumented with their own balance. The pressure field resulting from the loading on the blades determines part of the loading on the hub and spinner. Furthermore, for the presented cases where aerodynamic interaction occurs between the propellers, the flowfield experienced by the spinner and hub is a function of the loading on both propellers. Therefore, a blades-off tare would not be representative of the loading on the spinner and hub with blades installed.

Operating a propeller in a wind tunnel requires wall corrections. Methods for correction of propeller performance data at small and large angles of attack in the same wind tunnel are discussed in Ref. [46]. Corrections on advance ratio and propeller angle of attack were considered due to blockage from results of Sayers and Ball [47],

Downloaded by TU DELFT on August 19, 2021 | http://arc.aiaa.org | DOI: 10.2514/1.C035814

due to the sink effect of the propeller when operating at small angle of attack and due to the lift by the propeller when operating at large angle of attack following the method of Langer et al. [48]. While blockage for this experiment was negligible, a maximum advance ratio reduction of 1% should be considered by the reader in the interpretation of the uncorrected results due to the sink effect for the lowest J at $\alpha_p = 0$ deg and a maximum angle of attack reduction of 0.5 deg due to lift by the propeller for the lowest J at $\alpha_p = 95$ deg.

Total pressure measurements were performed behind the isolated propeller units to verify the F/T sensor thrust measurement; to verify the blade pitch setting of propeller unit B (without F/T sensor) through its thrust; and to establish a quantitative, time-averaged description of the slipstream flowfield. A total pressure probe was traversed through the slipstream just behind the propeller as shown in Fig. 2a and was connected to a digital pressure gauge with a range of −1000 to +3500 Pa and a full-scale accuracy of 0.03%. Measurements were taken for 10 s at a 3 Hz sampling frequency.

Additional flowfield measurements were taken in the wake of the rotors for the SBS configuration at $\alpha_p = 90$ deg using planar particle-image velocimetry (PIV). Figure 2b illustrates the positioning of the PIV measurement plane with respect to the models. Details of the measurement and postprocessing characteristics of the PIV setup are given in Table 1. Only phase-uncorrelated measurements were taken, with a total number of 1000 image pairs per measurement point to achieve convergence of the mean flowfields. Postprocessing was performed using an iterative multigrid approach [49], with a final window size of 16×16 pixels and 75% overlap. The resulting vector spacing of 0.4 mm was sufficient to characterize the slipstream development and identify the dominant flow structures in the wake of the propellers. The method by Wieneke [50] was used to calculate the uncertainty of the instantaneous velocity components, while the statistical uncertainty of the mean velocity components was obtained from the variations between uncorrelated samples at each vector location and the local number of samples available for averaging. This was calculated for the results at a medium propeller thrust level ($J = 0.62$). Table 1 includes the resulting uncertainty values averaged over the field of view. Note that the statistical uncertainty of the mean also contains a contribution due to turbulence (next to the contribution due to uncertainty of the instantaneous velocity fields).

Table 1 Measurement and postprocessing characteristics of the PIV setup

Parameter	Value
Laser	Nd:YAG 200 mJ
Cameras	2×5.5 Mpx
Objective	50 mm $f/8$
Field-of-view size	270×227 mm
Pulse separation	30 μs
Max. particle displacement	10 pixel
Image pairs	1000
Final interrogation window size	16×16 px
Window overlap factor	75%
Vector spacing	0.4 mm
Uncertainty instantaneous velocity	$0.050V_\infty$
Uncertainty mean velocity	$0.011V_\infty$

D. Test Cases

For this test campaign, the propeller blade pitch was set at $\beta_{0.7R_p} = 20.0$ deg to achieve considerable thrust for operation with freestream airspeed at zero propeller angle of attack but prevent significant flow separation on the blades at large angle of attack or at static condition. The selected freestream airspeed of $V_\infty = 20$ m/s was a compromise to achieve considerable thrust with the chosen blade pitch angle and to reduce wind-tunnel wall corrections, as for lower airspeeds the corrections become more significant. An overview of the test cases for the performance measurements is given in Table 2. The isolated propeller performance was measured at $V_\infty = 0$ m/s for $\alpha_p = 0$ deg and at $V_\infty = 20$ m/s for $0 \le \alpha_p \le 95$ deg. Propeller angle of attack α_p is defined with respect to the propeller axis like in Ref. [44]. Up- and downsweeps of propeller rotational speed were performed to vary helical tip Mach number M_{tip} at static condition and advance ratio when there was a freestream airspeed. Total pressure measurements in the slipstream of the isolated propeller in tractor and pusher configuration were performed at $V_\infty = 20$ m/s for $\alpha_p = 0$ deg.

All SBS and OAA configuration results were measured at a freestream airspeed of $V_\infty = 20$ m/s, and only corotating propellers were considered due to the limitations of the setup. For selected lateral distances d_y, the same range of angle of attack as for the isolated propeller was considered with the SBS configuration, measuring the rear propeller performance. A more extensive sweep of lateral distance of $2.1 \le d_y/R_p \le 6$ for rear propeller measurements and $2.1 \le d_y/R_p \le 4$ for front propeller measurements was performed at $\alpha_p = 90$ deg. For $d_y/R_p = 2.6$ at this angle of attack, PIV measurements of the slipstream interaction were taken. Both propellers were operated at the same rotational speed, except for two special cases with both propellers at equal thrust.

Although in a realistic application OAA interaction may only occur when the aircraft is at an angle of attack, all measurements for this configuration were performed at $\alpha_p = 0$ deg for simplicity. Two axial distances were considered, a far case at $d_x/R_p = 5.5$ and a close case at $d_x/R_p = 0.6$. The far case corresponds to the layout of the Airbus Vahana as sketched in Fig. 1b and, for example, the Joby S2 [12]. The close case is more relevant for propellers mounted with overlap or staggered on, for instance, the wing. The interaction for this case differs fundamentally from the far case, because the rear propeller experiences a slipstream that is not fully contracted yet. Lateral distances of $0 \le d_y/R_p \le 3$ were considered for the far case, and a smaller range of $1.28 \le d_y/R_p \le 3$ was considered for the close case, because for the latter the front propeller spinner was limiting any further overlap. The front propeller was operated at two different rotational speeds, and a sweep of rear propeller rotational speed was performed each time. Only the performance of the rear propeller was measured for the OAA configuration as for the main axial distance of interest, $d_x/R_p = 5.5$, the upstream effect was assumed to be negligible.

As the experimental data presented in this Paper can be useful for validation of numerical models, these data are provided in the supplements. The propeller performance data from the F/T sensor in the ISO, SBS, and OAA configuration is provided in Supplemental Data S3; in Supplemental Data S4, the slipstream total pressure measurements in the ISO configuration are given; and Supplemental Data S5 contains the planar PIV flowfield data in the SBS configuration.

Table 2 Overview of test cases for performance measurements

Configuration	F/T sensor location	V_∞, m/s	α_p, deg	d_x/R_p	d_y/R_p
ISO	ISO prop	0	0	— —	— —
ISO	ISO prop	20	0, 30, 60, 90, 95	— —	— —
SBS	Rear prop	20	0, 30, 60, 90, 95	— —	2.25, 4
SBS	Rear prop	20	90	— —	2.1, 2.25, 2.6, 3, 4, 6
SBS	Front prop	20	90	— —	2.1, 2.25, 2.6, 4
OAA	Rear prop	20	0	5.5	0, 0.25, 0.375, 0.5, 0.625, 0.75, 0.875, 1, 1.25, 1.5, 2, 3
OAA	Rear prop	20	0	0.6	1.28, 1.5, 1.75, 2, 3

prop = propeller.

Downloaded by TU DELFT on August 19, 2021 | http://arc.aiaa.org | DOI: 10.2514/1.C035814

Downloaded by TU DELFT on August 19, 2021 | http://arc.aiaa.org | DOI: 10.2514/1.C035814

III. Numerical Model

In the work of Usai [35], a blade element momentum (BEM) model was extended to include the effects of OAA propeller interaction. Results of this model are plotted alongside the experimental results in this Paper, to show that such a method can be used to predict performance and therefore be used for design purposes. The model consists of a few steps:

1) The front propeller loading distribution is determined with a BEM model.

2) The velocity distribution in the slipstream of the front propeller is calculated with a contraction model.

3) Induced velocities in the slipstream of the front propeller are superimposed on the rear propeller disk.

4) The rear propeller loading distribution is determined with a BEM model using the flowfield from step 3.

The blade element momentum model is based on the theory by Glauert [51] and uses the Prandtl tip and hub loss factors. Lift and drag predictions for each blade section were supplied from two-dimensional analyses with RFOIL [52] at the correct Reynolds number and Mach number. This viscous–inviscid coupled solver with Karman–Tsien compressibility correction, developed for wind turbine research, includes an estimation of the rotational effects experienced on a rotating blade by formulation of a quasi-three-dimensional system of boundary layer equations that include the leading terms due to rotation. Free transition from a laminar to a turbulent boundary layer was estimated with a critical amplification factor of 4, chosen based on the freestream turbulence level of the wind tunnel. In case of nonuniform inflow, quasi-steady results were calculated and then used as input to obtain an unsteady solution using nonstationary airfoil theory from Sears [53,54]. This was similarly applied by Ref. [37] for the unsteady blade response of a propeller in the wake of a pylon.

The slipstream estimated by momentum theory at the front propeller disk was contracted using a model from Chandrasekaran [55]. Given the flow characteristics at the front propeller disk, it was possible to compute the evolution of the slipstream geometry and axial and tangential velocity components along the slipstream axis. These were then interpolated to the rear propeller disk at the desired d_x and d_y distance. A BEM analysis with the same model resulted in the performance of the rear propeller. Any upstream effect on the front propeller was not accounted for. Further details of this extended BEM model can be found in Ref. [35].

IV. Results

The discussion of the results is divided in three parts, following the three propeller configurations: isolated, side-by-side, and one-after-another propeller configuration.

A. Isolated Propeller Configuration

The performance results of the isolated propeller configuration serve as the baseline for the other configurations. Furthermore, raw data from the F/T sensor are presented, and fits based on the raw data should establish confidence in the fitting procedure used in the remainder of the Paper. The correct operation of the F/T sensor is verified by comparison of the force in the thrust direction with the thrust estimated from integration of total pressure measurements in the propeller slipstream. Furthermore, the BEM model is validated in terms of isolated propeller performance. For propeller unit B (without the F/T sensor), verification of the thrust level is done by comparison of total pressure measurements in the slipstream with those for propeller unit A. This comparison is made with propeller unit B in both the tractor and pusher configurations. Finally, the influence of the fairing on the inflow to the pusher propeller and on its slipstream is investigated with total pressure measurements.

1. *Baseline Propeller Performance*

The baseline propeller performance at static condition ($V_\infty = 0$ m/s) is shown in Fig. 7. Furthermore, in Fig. 8, the performance at a freestream airspeed of $V_\infty = 20$ m/s is presented at various angles of attack from $\alpha_p = 0$ to 95 deg. In these plots, the raw F/T

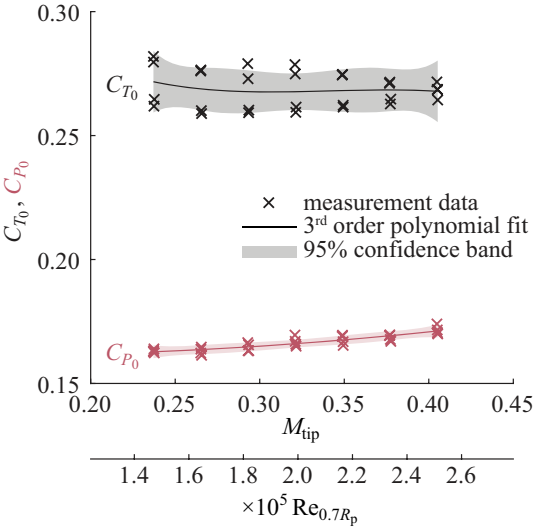

Fig. 7 ISO propeller thrust and power coefficient vs M_{tip} for $V_\infty = 0$ m/s, measured with the F/T sensor.

sensor data are shown, and third-order polynomial fits are presented, including 95% simultaneous confidence bands. Throughout the Paper, these fits are used to describe the propeller performance, and for those results, confidence intervals are shown based on these bands. In Fig. 7, results are plotted for a range of tip Mach number M_{tip} from 0.237 to 0.405, where M_{tip} was based on the rotational speed. The respective Reynolds number $Re_{0.7R_p}$ at the $r = 0.7R_p$ blade section is indicated as well for reference. While the thrust coefficient C_{T_0} is almost independent of M_{tip}, the power coefficient C_{P_0} increases slightly with increasing M_{tip}. Although the remainder of the Paper only shows results for $V_\infty = 20$ m/s, the propeller performance at static condition is a relevant reference, especially at large angle of attack, when the freestream axial velocity component [$V_a = V_\infty \cos(\alpha_p)$ in Fig. 9] for the propeller becomes small, zero, or even negative. Furthermore, the power at static condition serves as a baseline for eVTOL vehicles, similar to hover power for a helicopter. While the confidence band for C_{P_0} is very narrow, the C_{T_0} measurements are quite scattered and thus have a wider confidence band to consider. This is related to the sensor drift for which especially the thrust measurement is susceptible, as discussed in Sec. II.C. As can be observed, the measurements seem to form two groups, depending on whether an up- or downsweep in rotational speed was performed.

The isolated propeller performance for $V_\infty = 20$ m/s in Fig. 8 is used as the reference for the cases with interaction discussed in Secs. IV.B and IV.C. The propeller thrust and power coefficient C_T and C_P, the in-plane force coefficients C_{F_y} and C_{F_z} and the out-of-plane moment coefficients C_{M_y} and C_{M_z} are plotted versus advance ratio J. The three dashed lines of constant advance ratio at $J = 0.49$, 0.57, and 0.69 are the main conditions used in later results. Also, for this dataset, C_T has the widest confidence bands because of scatter in the data, followed by those for C_{F_y}. All other quantities have significantly less scatter as they are less prone to sensor drift. At zero angle of attack, C_T decreases with increasing J. For a given J, C_T increases with increasing α_p, until from a certain α_p, in this case around 60 deg, the $C_T - J$ curve slope changes sign. When one would extend the curves for different α_p to the left, they seem to merge at a level very similar to C_{T_0} from Fig. 7. The behavior of C_P with variation of J and α_p is similar to that of C_T, albeit at a different level.

To understand the interaction phenomena in later sections, an understanding of the effects of α_p on propeller performance is required, and therefore a short discussion is included. In Fig. 9a, a sketch is shown to illustrate the effects. The velocity component of the freestream normal to the propeller axis, $V_n = V_\infty \sin(\alpha_p)$, results in an asymmetric inflow condition. Blade sections on the advancing blade side experience an increased angle of attack, increasing thrust (Fig. 9d). On the retreating blade side, the reverse occurs, reducing

Downloaded by TU DELFT on August 19, 2021 | http://arc.aiaa.org | DOI: 10.2514/1.C035814

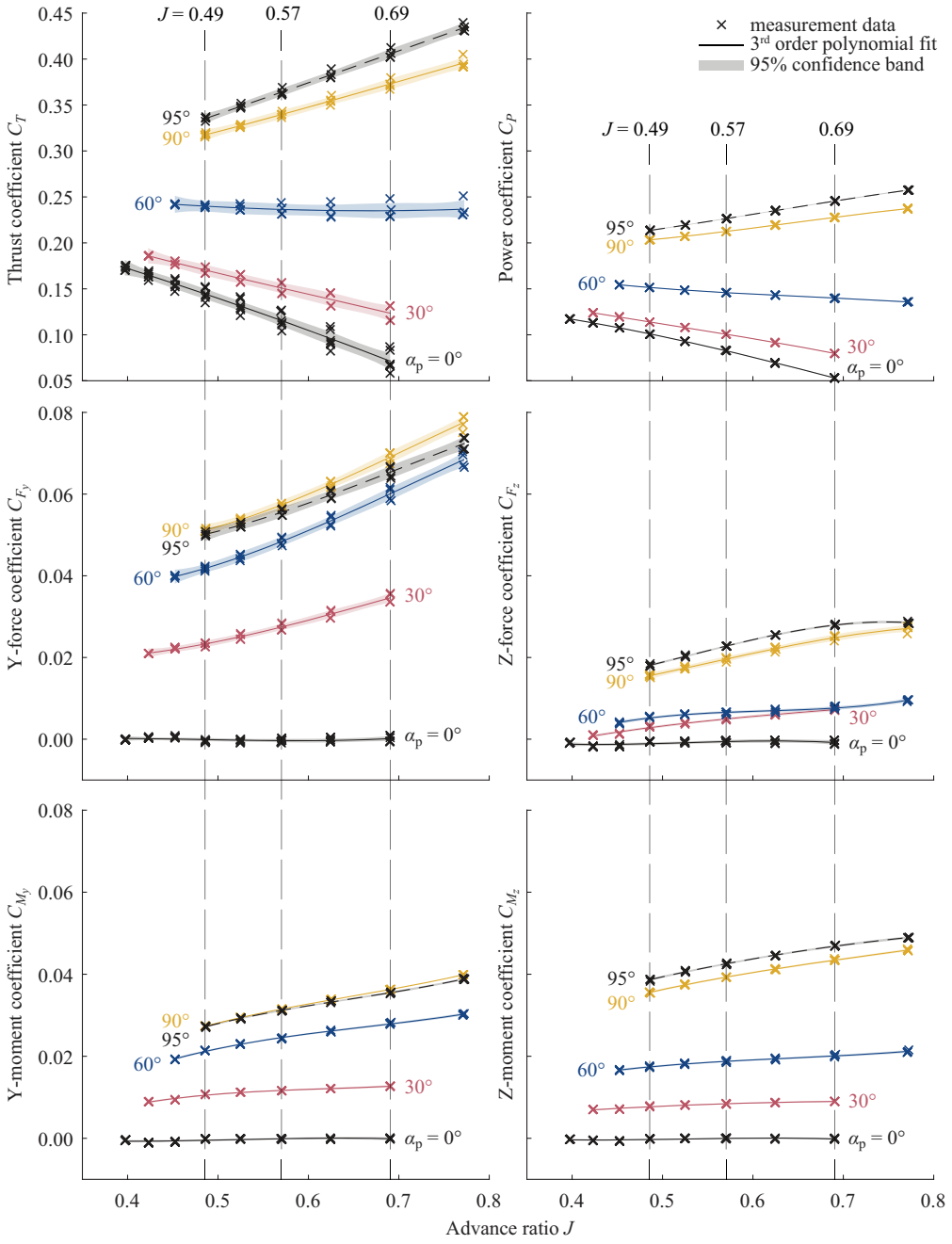

Fig. 8 ISO propeller performance vs J at various propeller angles of attack for $V_\infty = 20$ m/s, measured with the F/T sensor.

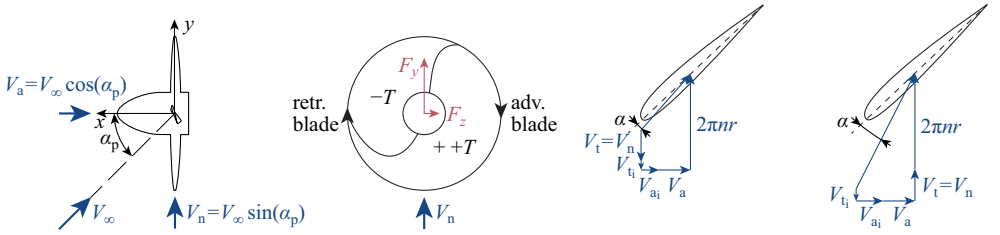

Fig. 9 Sketch showing the typical effect of angle of attack on propeller forces, relative to propeller at $\alpha_p = 0$ deg, including velocity triangle for retreating (retr.) and advancing (adv.) blade section with induced velocity components V_{a_i} and V_{t_i}.

thrust (Fig. 9c). However, this is not exactly the opposite of the impact on the advancing blade side as the effective velocity is reduced as well. With increasing α_p, the axial component of the freestream, $V_a = V_\infty \cos(\alpha_p)$, decreases. This results in a uniform increase in blade section angle of attack over the propeller disk, increasing thrust. The net combined result is an increase in thrust with α_p, composed of a slightly reduced thrust on the retreating blade side ($-T$ in Fig. 9b) and strongly increased thrust on the advancing blade side ($++T$ in Fig. 9b). A discussion of these effects can also be found in the work by Ortun et al. [45] and Veldhuis [56].

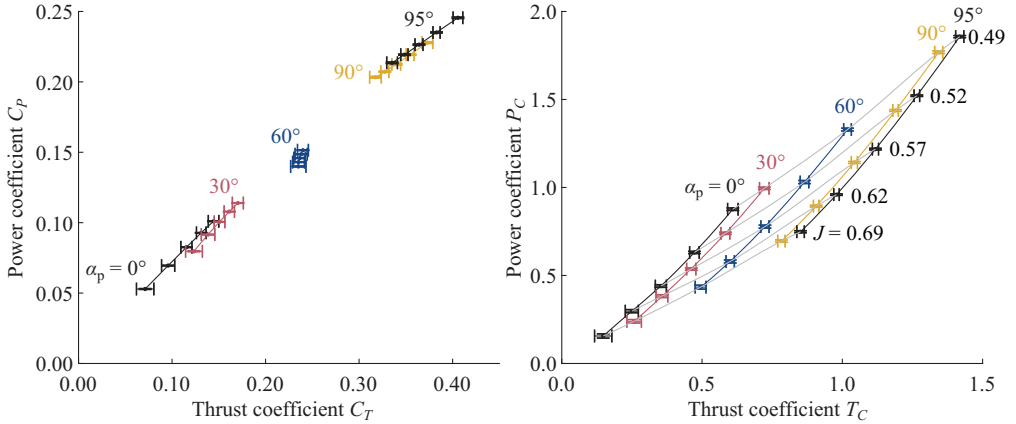

a) Power versus thrust coefficient based on n **b) Power versus thrust coefficient based on V_∞**

Fig. 10 ISO propeller power vs thrust at various J and propeller angles of attack for $V_\infty = 20$ m/s, measured with the F/T sensor.

Downloaded by TU DELFT on August 19, 2021 | http://arc.aiaa.org | DOI: 10.2514/1.C035814

While C_T and C_P are very relevant for vehicle performance, the in-plane forces and out-of-plane moments can be relevant for vehicle stability. The in-plane force component in the direction of the angle of attack, defined as the y-force coefficient C_{F_y} by the axis system shown in Fig. 5a, is zero at zero α_p and increases with increasing α_p. The mechanism behind this is the asymmetry in thrust formed over the propeller disk as was shown in the sketch in Fig. 9. The asymmetry in thrust between the advancing and retreating blade side is accompanied by a similar asymmetry in tangential forces, resulting in a net y-force. C_{F_y} increases relatively more with angle of attack for higher J, as the freestream airspeed becomes relatively more important for the blade loading when the rotational speed decreases. A significant positive component of this force coefficient can also be caused by loading on the spinner as a result of the skewed inflow. Spinner in-plane forces are discussed by Ortun et al. [45].

The other in-plane force coefficient C_{F_z} is much smaller than C_{F_y}. Because of a phase lag in the blade loading change, part of the retreating blade side experiences increased thrust, and part of the advancing blade side experiences decreased thrust. This is made visible in the sketch in Fig. 9b by the curvature in the dividing line between the $-T$ and $++T$ regions. The dominating mechanism behind this phase lag is variations in induced velocity across the propeller disk [45]. The tangential force components in these regions sum up to a net positive z-force. Also, this force coefficient can have a contribution from the spinner, in this case resulting from the asymmetry in static pressure field between the advancing and retreating blade side [45,46]. This effect can decrease or increase C_{F_z} depending on the upstream and downstream extent of the spinner from the propeller plane. The asymmetry in loading on the propeller disk with angle of attack also results in nonzero out-of-plane moment coefficients C_{M_y} and C_{M_z}, which correlate to C_{F_y} and C_{F_z}, respectively. However, the nonzero out-of-plane moment coefficients are caused by the asymmetry in the thrust component instead of the tangential force component.

To investigate the relation between thrust and power with varying J and α_p, in Fig. 10, the power coefficient is plotted versus thrust coefficient, made dimensionless with the rotational speed in Fig. 10a and with the freestream airspeed in Fig. 10b. In the C_P–C_T plot, the data collapse approximately to an almost linear line; in other words, variations in J and α_p only marginally affect the $C_T - C_P$ ratio for the presented conditions. As rotational speed was varied to change advance ratio and the freestream airspeed was constant, the $P_C - T_C$ plot is more indicative of propeller performance. It can be seen that with increasing α_p the power required by the propeller reduces for a given thrust level.

2. *Verification of F/T Sensor Measurements and Validation of BEM Model*

The F/T sensor data were verified by comparison with total pressure measurements in the propeller slipstream. Figure 11 presents the

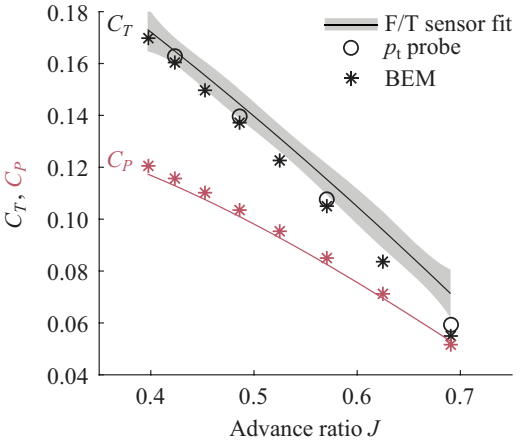

Fig. 11 Comparison of measured and predicted ISO propeller performance for $V_\infty = 20$ m/s and $\alpha_p = 0$ deg.

fitted F/T sensor data for C_T and C_P at $\alpha_p = 0$ deg together with C_T values obtained from the total pressure wake measurements. A sweep of total pressure measurements was performed in a single radial direction at $x/R_p = 0.48$ behind the propeller, and the corresponding results are shown in Fig. 12. To obtain a thrust force from these total pressure measurements, the same radial total pressure distribution was assumed at each azimuthal location, in other words, an

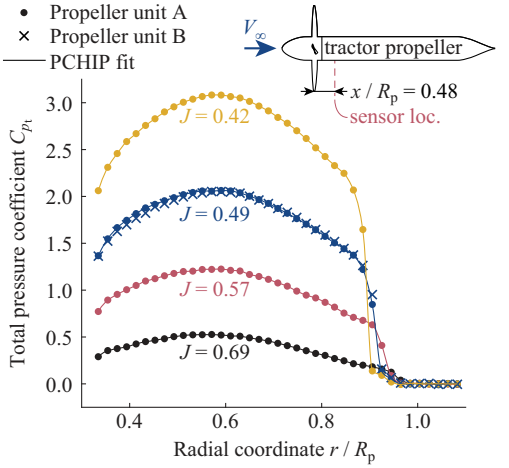

Fig. 12 Radial distribution of C_{p_t} at $x/R_p = 0.48$ at single azimuthal location (loc.) behind the two propeller units for $V_\infty = 20$ m/s and $\alpha_p = 0$ deg with piecewise cubic Hermite interpolating polynomial fit.

Downloaded by TU DELFT on August 19, 2021 | http://arc.aiaa.org | DOI: 10.2514/1.C035814

axisymmetric slipstream. A thrust force was obtained by integration of the total pressure, with the freestream total pressure subtracted, over the slipstream cross-section. This thrust estimation from the total pressure data was then corrected to account for the contraction effect. First, the local slipstream radius R_{sl} at the total pressure measurement plane was estimated from the radial distribution of total pressure coefficient in Fig. 12. R_{sl} was estimated by drawing a tangent through the point of steepest descent of the piecewise cubic Hermite interpolating polynomial (PCHIP) fit of the data and finding the intersection with $C_{p_t} = 0$. The integrated thrust was then corrected by multiplication with the area ratio $\pi R_p^2/\pi R_{sl}^2$.

The C_T values calculated from the total pressure measurements in Fig. 11 compare reasonably well with those from the F/T sensor, although a nonnegligible offset can be observed, especially toward the highest J. The total pressure measurements do not account for any spinner loading effects, and very close to the nacelle, no pressure measurement was done, both leading to an error in C_T. Furthermore, the contraction correction may have introduced an error as well. The F/T sensor data confidence bands are quite large, indicating an uncertainty in the measured C_T as well. Overall, the reasonable agreement verifies the correct operation of the F/T sensor. In Fig. 11, also results from the BEM model are included to validate the performance predictions by this model. The BEM model predictions agree well with the F/T sensor data in terms of C_P. In terms of C_T, an offset is visible, especially toward the highest J. Part of the offset may be a result of spinner loading as the BEM model prediction does not include spinner loading. This BEM model is used in Sec. IV.C for performance prediction of the OAA configuration.

3. *Performance Verification of Propeller Unit B (Without F/T Sensor)*

Four radial sweeps of total pressure coefficient were obtained behind propeller unit A (with the F/T sensor) for different J. These sweeps are shown in Fig. 12. For $J = 0.49$, a C_{p_t} sweep is also plotted that was measured behind propeller unit B (without the F/T sensor). Good agreement between the measurements behind the two propeller units is obtained, with a difference in thrust of 0.4%, indicating a correct blade pitch angle setting on unit B. For this condition, maximum C_{p_t} is found around $r/R_p = 0.6$. Contraction of the slipstream, for which a correction of the data was needed to obtain integrated thrust, is clearly visible when looking at the edge of the slipstream, especially at high loading conditions. Therefore, the maximum thrust on the blade is more outboard from the radial location of the maximum C_{p_t}.

4. *Comparison of Pusher and Tractor Propeller Performance*

When propeller unit B was used in the pusher configuration, the blades were turned by 180 deg, necessitating again verification of the thrust level. However, the pusher propeller sees a different inflow than the tractor propeller, because its inflow is disturbed by the wakes of the nacelle and pylon with fairing, complicating the comparison. Furthermore, the development of the slipstream for the pusher propeller is different from that of the tractor propeller because for the pusher propeller the spinner contracts, while the nacelle behind the tractor propeller has a constant radius in the vicinity of the propeller. Despite these complicating factors, in Fig. 13a, comparison was made of C_{p_t} in the lip stream of the pusher and tractor propeller. A total pressure measurement sweep was performed in a direction perpendicular to the pylon and fairing, reducing the effect they may have on the local slipstream flowfield. Note that the distance of the total pressure probe behind the propeller for the pusher propeller is not exactly the same as for the tractor propeller. Instead, it was chosen to coincide with the location of the rear propeller for the OAA configuration at close d_x. Although increased contraction can be seen for the pusher propeller, partially forced by the contraction of the spinner, the maximum in C_{p_t} is very similar to that of the tractor propeller for the two advance ratios. The integrated difference in thrust is $+0.8\%$ at $J = 0.57$ and -0.6% at $J = 0.49$, confirming the correct setting of blade pitch angle of the propeller unit in the pusher configuration.

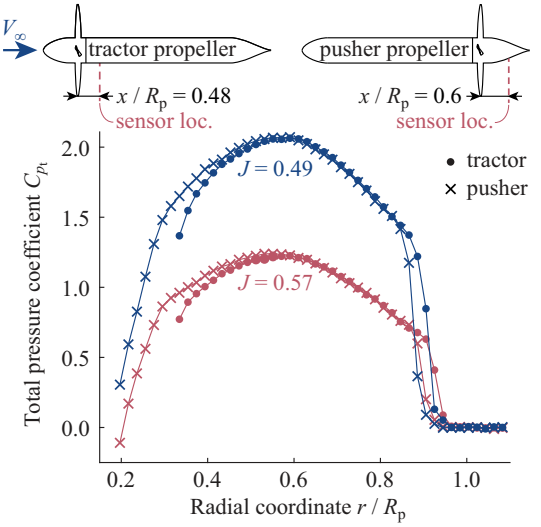

Fig. 13 Comparison of radial distribution of C_{p_t} in the slipstream of the pusher and tractor propeller for $V_\infty = 20$ m/s and $\alpha_p = 0$ deg.

Although for the OAA configuration a pusher propeller was chosen as the front propeller to avoid having the pylon and fairing in the slipstream, the effect of the pylon and fairing on the slipstream is not negligible. This is illustrated in Fig. 14 using total pressure measurements. The first comparison is between a lateral pressure sweep $0.7R_p$ below and above the propeller center at a distance of $x/R_p = 0.6$ behind the propeller. In the lower sweep (x symbol), the effect of the fairing is visible by a drop in total pressure at slightly negative$y$ coordinate. This drop in total pressure is a result of the drop in total pressure in the wake of the fairing, that is only partially compensated by the increase in total pressure from the propeller: The thrust and thus the total pressure jump by the propeller are locally higher as a result of the reduced axial inflow velocity from the wake. The shift to negative$y$ coordinate is a result of the swirl component in the slipstream, displacing the fairing effect in azimuthal direction. The effect of the upstream fairing on the slipstream characteristics is, however, not very pronounced and thought to be less pronounced than the reverse setup with a tractor propeller and fairing in the slipstream, as for such a setup the fairing wake is not partially filled by the propeller and the swirl in the slipstream is locally reduced by the fairing.

Figure 14 also shows the total pressure in a sweep across the propeller center at a distance of $x/R_p = 5.5$. This measurement coincides with the rear propeller location for the OAA configuration at the far d_x and is shown to quantify the inflow experienced by the downstream propeller in this configuration. Comparing the total pressure at negative and positive$y$ coordinate, a slight asymmetry of the slipstream edge can be observed. This could have been introduced by the fairing. In the slipstream core, no total pressure measurement was possible with the used probe due to vibrations. Most likely, in this area, a hub vortex is formed from the blade root vortices. When comparing the slipstream edge in this figure at $d_x/R_p = 5.5$ with the measurements in Fig. 13 at $d_x/R_p = 0.6$, an increased slipstream contraction is clearly present at $d_x/R_p = 5.5$. This will have an influence on the OAA interaction, that was studied with the rear propeller at both axial distances.

B. Side-by-Side Propeller Configuration

This section discusses the results of one of the main interaction cases identified in this Paper: side-by-side propeller interaction. This interaction type is of importance especially in the transition phase of eVTOL vehicles, when propeller thrust is used for lift when transitioning from climbing flight to forward flight. During this maneuver, large changes in propeller angle of attack occur, altering the direction of the slipstreams and as such the effects of aerodynamic interaction between the propellers. First, results are presented where both

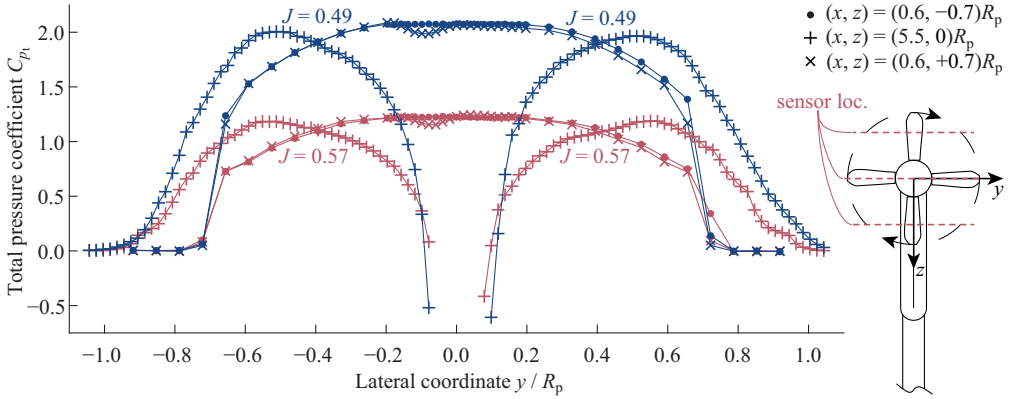

Fig. 14 Lateral distribution of C_{p_t} at $x/R_p = 0.6$ behind the pusher propeller for data $0.7R_p$ below and above the propeller center and at $x/R_p = 5.5$ for data across the center, for $V_\infty = 20$ m/s and $\alpha_p = 0$ deg.

propellers operate at equal advance ratio, calculated using the free-stream velocity and the rotational speed of each propeller. Second, results are shown for which the propellers operate at equal thrust or combined constant thrust, compensating for interaction effects. This enables the determination of required power changes to maintain thrust.

1. *Propellers at Equal Advance Ratio*

In Fig. 15a, performance comparison is plotted between the ISO configuration and SBS configuration as a function of α_p at $V_\infty = 20$ m/s and $J = 0.57$. This figure is meant to illustrate propeller interaction during the transition phase for eVTOL vehicles, where $\alpha_p = 0$ deg represents takeoff and $\alpha_p = 95$ deg forward flight with an aircraft angle of attack of 5 deg; see Fig. 5c. Although in a realistic scenario the inflow velocity to the propeller during transition is not constant and blade pitch and/or rotational speed may be adjusted to meet the required performance, for simplification, the operating conditions were kept constant. In case of the SBS configuration at nonzero α_p, performance is plotted of the rear propeller because for this propeller more significant interaction effects can be expected than for the front one. Two distances d_y were considered to highlight the sensitivity of the interaction to the propeller spacing. At $\alpha_p = 0$ deg, no significant performance effects can be observed as a result of SBS interaction. With increasing angle of attack, an increasing reduction in C_T and C_P with respect to the isolated propeller can be noticed for the rear propeller in SBS interaction. As expected, this decrease is worse for the propellers at close distance $d_y/R_p = 2.25$ than at the further distance $d_y/R_p = 4$. A maximum in C_T and C_P occurs around $\alpha_p \approx 90$–95 deg for the SBS case, while for the ISO configuration, both performance parameters increase significantly in value beyond $\alpha_p = 90$ deg. As will be shown by the PIV results later, the mechanism behind this reduction in C_T and C_P for the rear propeller is likely a reduction of effective α_p as a result of operating in the downwash of the front propeller, similar to what was found for

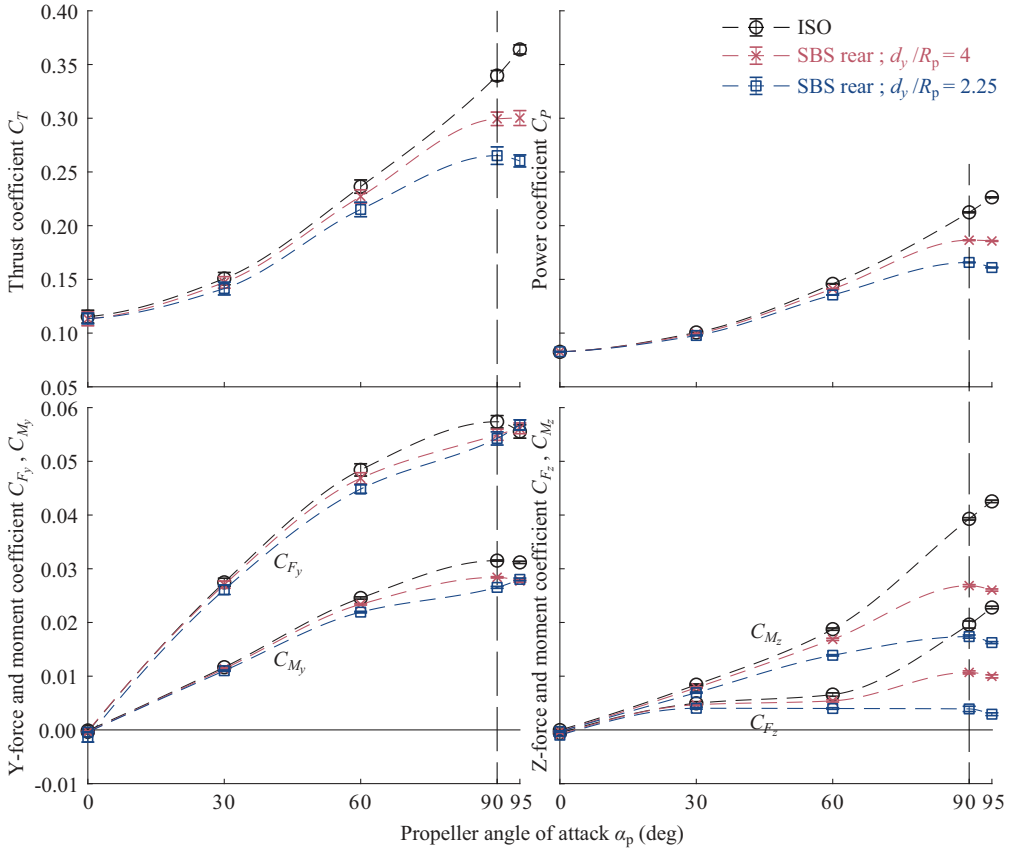

Fig. 15 ISO and SBS rear propeller performance vs α_p for $V_\infty = 20$ m/s and $J = 0.57$, fitted from F/T sensor data.

Downloaded by TU DELFT on August 19, 2021 | http://arc.aiaa.org | DOI: 10.2514/1.C035814

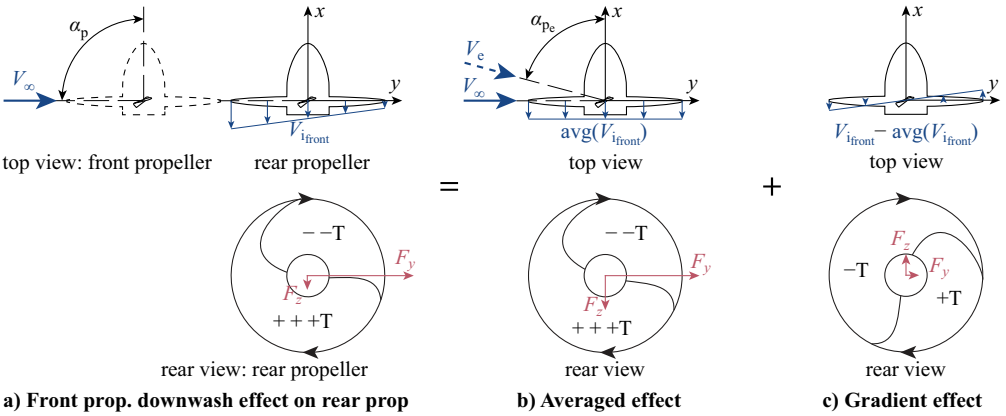

Fig. 16 Sketch showing the typical effect of SBS interaction on rear propeller (prop.) forces at $\alpha_p = 90$ deg, relative to isolated propeller at $\alpha_p = 0$ deg.

tandem rotors by Refs. [22,23]. This situation is sketched in Fig. 16a for $\alpha_p = 90$ deg. The averaged effect of the downwash is a reduction in α_p as shown in Fig 16b. The effective angle of attack can be estimated from isolines of C_T and C_P (horizontal lines in Figs. 15a and 15b). For $\alpha_p = 95$ deg and $d_y/R_p = 4$, the effective angle of attack is estimated to be 15 deg less than the geometric, while for $d_y/R_p = 2.25$, it is even 27 deg less.

The in-plane force coefficients C_{F_y} and C_{F_z} and out-of-plane moment coefficients C_{M_y} and C_{M_z} are also plotted in Fig. 15. For $\alpha_p \leq 60$ deg, the effect of SBS interaction on C_{F_y} of the rear propeller is similar to the effect on C_T. However, the results at $\alpha_p = 90$ and 95 deg do not follow the trend of increased reduction with angle of attack. A crossover point can even be noticed near $\alpha_p = 95$ deg where C_{F_y} of the rear propeller in SBS interaction becomes larger than that of the ISO propeller. C_{M_y} follows the trend of C_{F_y} as it is a derivative effect, except for the crossover. On the other hand, the effect of SBS interaction on C_{F_z} and C_{M_z} of the rear propeller is similar to the effect on C_T but amplified. To explain the interaction effects on C_{F_y} and C_{F_z}, the sketch in Fig. 16 is again used. From the fact that the interaction effects more downstream at $d_y/R_p = 4$ are smaller than at $d_y/R_p = 2.25$, it can be implied that the rear propeller sees a nonconstant distribution of downwash in the y direction, reducing with increasing distance from the front propeller. The gradient of downwash with respect to y likely results in the secondary effect sketched in Fig. 16c, in which the thrust is relatively decreased on the side of the propeller disk closest to the front propeller and relatively increased on the side that is farther away. This asymmetry in thrust and the corresponding asymmetry in tangential forces causes a negative force contribution in the z direction, opposing the z force for the isolated propeller at angle of attack. A phase lag in this asymmetry can result in a positive force contribution in the y direction, possibly explaining the crossover in C_{F_y} occurring at large angle of attack. It is thought that this phase lag originates from variations in induced velocity across the propeller disc similar to the phase lag in loading for a propeller at angle of attack [45].

At $\alpha_p = 90$ deg, dashed lines are drawn in Fig. 15 for which in Fig. 17 performance plots are presented as function of d_y. In this figure, the performance quantities are expressed as ratios between the quantity in interaction and the quantity for the isolated propeller at the same operating condition. Results are shown for both the rear and front propellers, as the propeller units were switched around in the experiment, at three advance ratios $J = 0.49$, 0.57, and 0.69. While for the rear propeller C_T reduces as a result of the SBS interaction, for the front propeller, a small increase is noticeable at small d_y. As was found by Refs. [22,23] for a tandem rotor, an upwash from the rear propeller slightly increases the front propeller angle of attack. The effect of the interaction for the rear propeller is dependent on the advance ratio, increasing in strength with increasing advance ratio, or decreasing rotational speed. This is explained by the increased gradient of $C_T - \alpha_p$ at higher advance ratios for the isolated propeller as is shown in Fig. 8. While the effect of interaction on the front propeller becomes negligible when d_y increases to 4, the effect on the rear propeller remains significant for the plotted range up to $d_y/R_p = 6$. Apparently, the effective change in angle of attack by the front propeller extends far downstream. Exactly the same effects are seen for C_P.

As was discussed in relation to Fig. 15, the SBS interaction effect for C_{F_y} is smaller than for C_T for the rear propeller. Figure 17 shows that this conclusion is true for the whole tested range of d_y. The trend of interaction effect with advance ratio is reversed compared to that for C_T. For the highest plotted advance ratio, C_{F_y} is even slightly increased with respect to the isolated configuration. This is explained by the fact that a propeller operating at higher J is relatively more influenced by inflow velocity changes, like the interaction effect sketched in Fig. 16c that is thought to increase C_{F_y}. In line with C_T, the interaction effect on the front propeller is small for C_{F_y}. Similar results are shown for C_{M_y}.

For C_{F_z}, the interaction effect is stronger than for C_T for the whole range of d_y. At $d_y/R_p = 2.1$, the force component is reduced to just 20% of its value without interaction. However, the absolute values are relatively small compared to the other force components. The effect on the front propeller is again small. C_{M_z} follows the trends of C_{F_z}.

Considering the large discovered effects on the propeller forces and moments, SBS interaction can have significant consequences for the aircraft stability. This, however, very much depends on the location of the rear propeller with respect to the center of gravity. If thrust is lost at a far distance from the center of gravity, its moment arm can induce a pitch-up or pitchdown moment. The dependency of the interaction effect on d_y and the direct dependency of stability on the rear propeller location through d_y make it also hard to draw any general conclusions. However, the found interaction results enable the reader to make a first estimate of stability effects for specific eVTOL layouts.

For the lowest and highest advance ratios plotted in Fig. 17, at $d_y/R_p = 2.6$ the time-averaged slipstream flowfield in a plane perpendicular to the propeller disk and parallel to the freestream velocity is shown in Fig. 18, as measured with the PIV setup (Sec. II.C). Note that this velocity field only contains the in-plane velocity components and the out-of-plane component is not included. For both advance ratios, a mixing of the front and rear propeller slipstreams can be observed. As expected, for lower J, the impingement of the front propeller slipstream on the rear propeller slipstream happens more downstream. This is a result of the higher induced axial velocity due to the higher thrust at lower J. Despite the lower thrust of the rear propeller as a result of the interaction, the rear propeller slipstream seems to form an angle with the propeller rotation axis equal or smaller than for the front propeller. This indicates that the effective angle of attack for the rear propeller is indeed reduced by the downwash of the front propeller, confirming the mechanism sketched in Fig. 16. Another observation is that the velocity distribution in the slipstreams is rather nonuniform. This is likely induced by the very nonuniform loading on the propeller due to this skewed inflow. Note

Downloaded by TU DELFT on August 19, 2021 | http://arc.aiaa.org | DOI: 10.2514/1.C035814

Downloaded by TU DELFT on August 19, 2021 | http://arc.aiaa.org | DOI: 10.2514/1.C035814

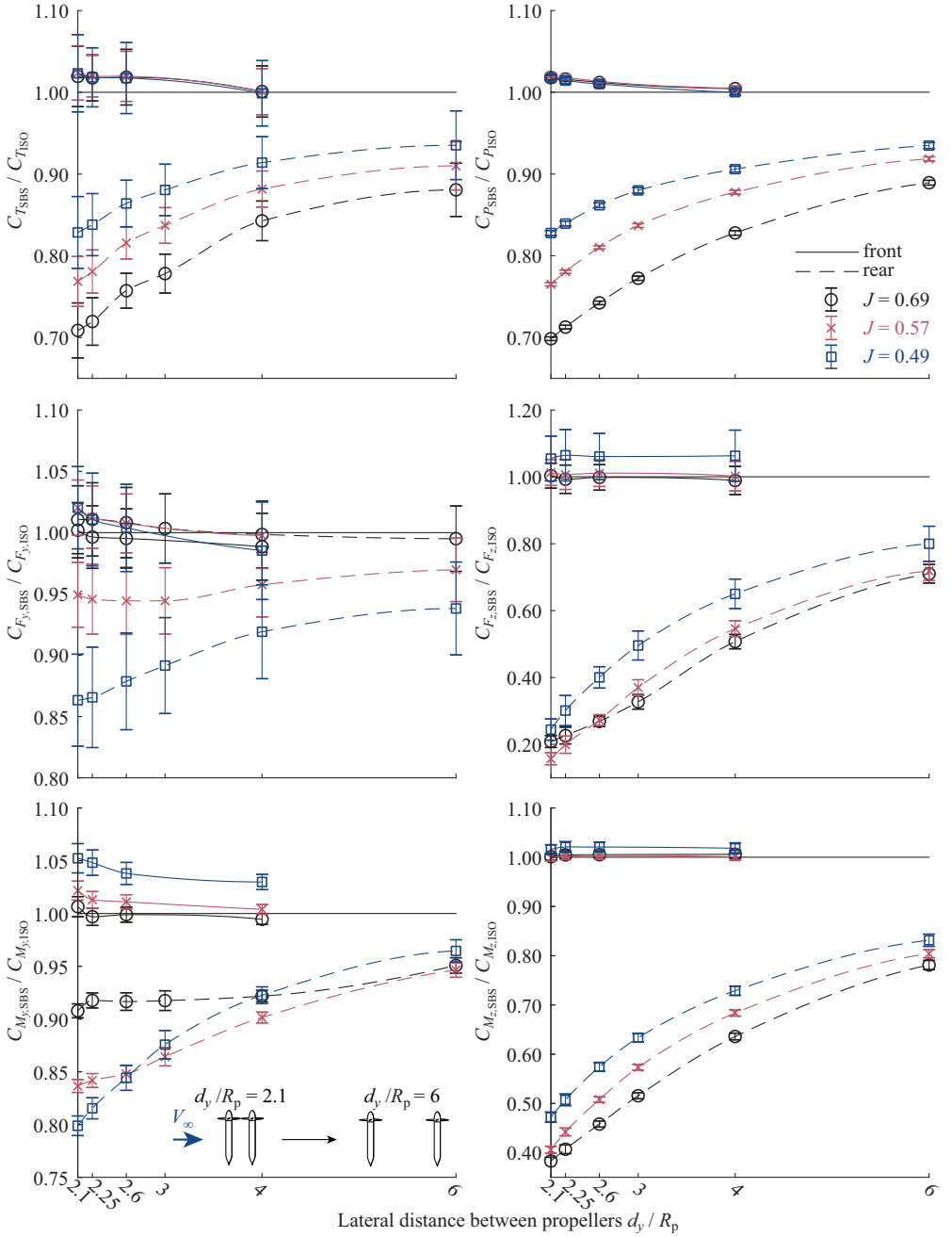

Fig. 17 Front and rear propeller performance change due to SBS interaction as function of d_y for $V_\infty = 20$ m/s and $\alpha_p = 90$ deg (forward flight) at three advance ratios, fitted from F/T sensor data.

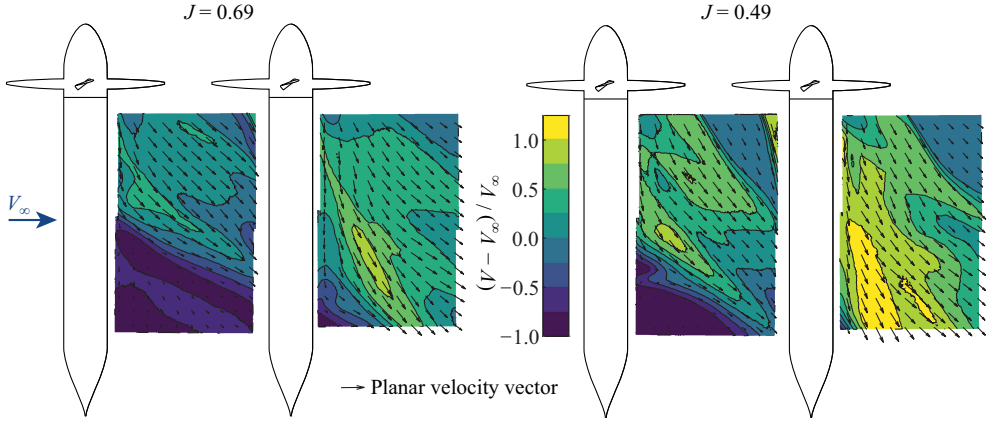

Fig. 18 Time-averaged flowfield from planar PIV measurements behind propellers in SBS interaction for $V_\infty = 20$ m/s, $\alpha_p = 90$ deg, and $d_y/R_p = 2.6$.

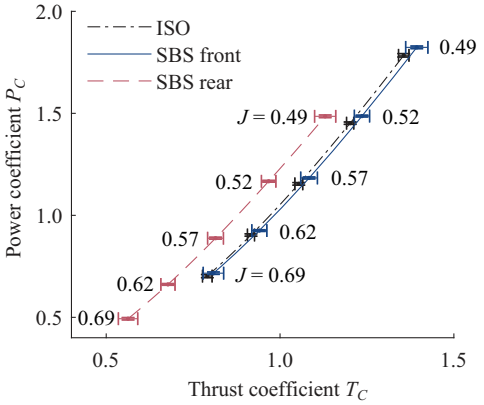

Fig. 19 ISO and SBS front and rear propeller power versus thrust coefficient for $d_y = 2.1$, $V_\infty = 20$ m/s, and $\alpha_p = 90$ deg, fitted from F/T sensor data.

that below the propeller slipstreams large velocity deficits are noticeable in the PIV measurements, which are the wakes of the nacelles.

Figure 17 does not directly highlight any changes in propeller efficiency. Therefore, in Fig. 19, a $P_C - T_C$ plot is given for the ISO and SBS configurations at $d_y/R_p = 2.1$ and $\alpha_p = 90$ deg. Note that, because in the SBS configuration the front and rear propellers are in aerodynamic interaction and their advance ratio was kept equal, the results for the front and rear propeller can only be compared at constant advance ratio. However, comparison with the ISO configuration is valid for unequal advance ratio. Clearly, for a given T_C, a higher shaft power is required for the SBS rear propeller compared to the ISO configuration, while for the SBS front propeller, the required power reduces slightly. The shift between the ISO and the SBS rear result is very similar to a decrease in propeller angle of attack in Fig. 10b, while the shift between the ISO and the SBS front result resembles an angle of attack increase. Further analysis on the efficiency is done in the next section by keeping thrust constant between the front and rear propellers.

2. *Propellers at Equal Thrust*

To assess the effects of SBS interaction on the power demand, the lost thrust due to interaction for the rear propeller needs to be compensated. For $\alpha_p = 90$ deg and $d_y/R_p = 2.6$, an experiment was performed where the rotational speed of the front propeller was fixed at two specific advance ratios, $J = 0.77$ and $J = 0.62$, and the rotational speed of the rear propeller was varied to obtain the same thrust as the front propeller. T_C was used instead of dimensional thrust to remove any effects of change in freestream temperature or static pressure during the experiment. The front propeller T_C was assumed to be equal to that found with the rear propeller at the same J, thus ignoring the secondary effect of the increase in rear propeller thrust on the front propeller loading. For $J = 0.77$, an increased power of 7.3% was found due to the interaction effect for the propellers combined. For $J = 0.62$, this was slightly lower at 5.8%. For the latter advance ratio, the slipstream flowfield is visualized in Fig. 20, for both equal advance ratio and equal thrust. The rear propeller slipstream for the case at equal thrust forms an even smaller angle with respect to the propeller rotation axis. This shows that the decreased deflection with decreasing J observed in Fig. 18 not only depends on the front propeller setting and the resulting downwash on the rear rotor (mechanism sketched in Fig. 16) but also on the rear propeller setting. When the propellers are operating at equal thrust, the slipstream deflection difference between the front and rear propellers is even larger than when operating at equal advance ratio, indicating again a reduced effective angle of attack for the rear propeller.

A second strategy that can be thought of to maintain equal thrust compared to the situation without interaction is to keep the front and rear propellers operating at equal advance ratio but to reduce this advance ratio to compensate for the loss in combined thrust. The reference thrust in this case is chosen to be the thrust of the isolated propeller at $J = 0.62$, $V_\infty = 20$ m/s, and $\alpha_p = 90$ deg, so the same reference condition as in the previous paragraph. For this analysis, the front propeller performance is assumed equal to the isolated propeller performance. In Fig. 21, the power at this thrust is plotted for three cases: the ISO propeller configuration and the average of the front and rear propellers in SBS configuration with $d_y/R_p = 4$ and $d_y/R_p = 2.25$. The power is plotted relative to the isolated propeller power at static condition at the same thrust, so a value higher than 1 means more power is required than hover power. For the ISO configuration, at $\alpha_p = 0$ deg and 40% more power is required than hover power because the freestream velocity of $V_\infty = 20$ m/s can be seen as a climbing flight. This power requirement reduces with increasing α_p to a situation where only 80% of the hover power is required at $\alpha_p = 95$ deg. With interaction, a similar trend is followed, but at reduced slope, meaning that especially at large α_p the SBS interaction results in a power penalty with respect to the ISO configuration of up to 8.0 and 13.2% at $\alpha_p = 95$ deg for $d_y/R_p = 4$ and $d_y/R_p = 2.25$, respectively. In any case, SBS interaction is neutral or detrimental for the performance.

C. One-after-Another Propeller Configuration

This section discusses the results of the second interaction case identified in this Paper: one-after-another propeller interaction. This interaction type is of importance especially in cruise flight of eVTOL vehicles, where propeller thrust is used to propel the vehicle. While in the design cruise condition of eVTOL vehicles the slipstream of one propeller may not impinge on another propeller, during maneuvers or due to angle of attack changes, such situations may arise. An analysis of the performance effects characteristic of this interaction is therefore important. First, results are presented for the case with both propellers operating at equal advance ratio. Second, results are shown for the case

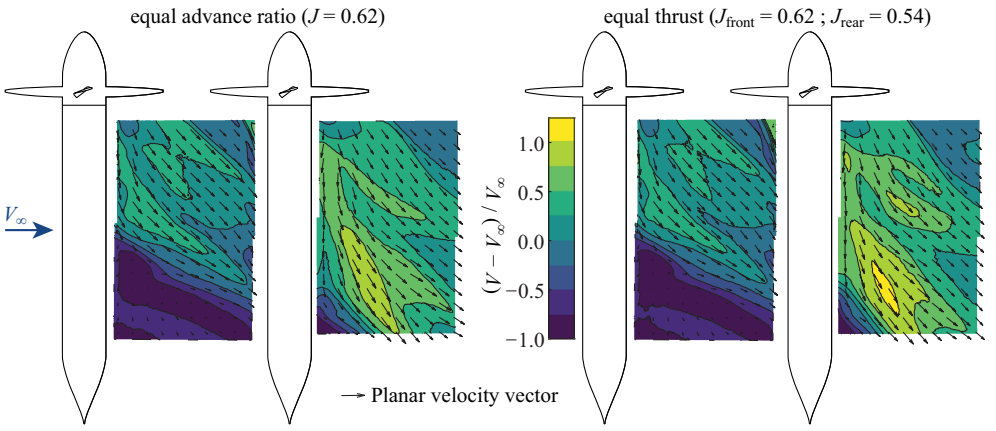

Fig. 20 Time-averaged flowfield from planar PIV measurements behind propellers in SBS interaction at equal J and equal thrust ($T_C = 0.93$) for $V_\infty = 20$ m/s, $\alpha_p = 90$ deg, and $d_y/R_p = 2.6$.

Downloaded by TU DELFT on August 19, 2021 | http://arc.aiaa.org | DOI: 10.2514/1.C035814

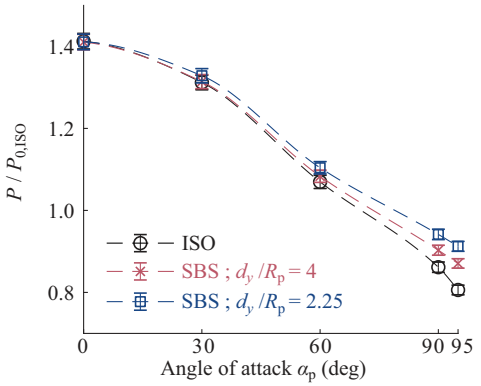

Fig. 21 Power in three scenarios at equal thrust ($T_C = 0.93$) for $V_\infty = 20$ m/s, fitted from F/T sensor data: the ISO propeller and the average of the front and rear propeller in SBS interaction at $d_y/R_p = 4$ and 2.25.

with the propellers operating at equal thrust, in order to determine the required power change compared to the situation without interaction. Results are shown for two axial distances between the propellers, a far case with $d_x/R_p = 5.5$ and a close case with $d_x/R_p = 0.6$. The far case represents, for instance, interaction found between a propeller mounted on a wing and one on a tailplane. The close case is representative for propellers mounted with an overlap on for instance the wing leading edge. The interaction effects in this section are limited to the effects for the rear propeller. Predictions of the interaction effects on thrust and power with the extended BEM model are shown alongside the experimental results.

1. *Propellers at Equal Advance Ratio*

In Fig. 22, the thrust and power coefficient of the rear propeller in OAA interaction are plotted as function of lateral distance d_y for two advance ratios $J = 0.57$ and $J = 0.49$. The performance is plotted as a ratio with the isolated performance in the denominator. Results are shown for both the far and close case with $d_x/R_p = 5.5$ and $d_x/R_p = 0.6$, respectively. Measurements are shown in Fig. 22a, and predictions with the extended BEM model are shown in Fig. 22b. For the farthest lateral distance, $d_y/R_p = 3$, no significant interaction effect on C_T and C_P was measured. The BEM model prediction is in agreement because with its formulation the rear propeller sees an undisturbed freestream inflow for this d_y. For $d_x/R_p = 5.5$, the interaction effect is still negligible when the lateral distance is decreased to $d_y/R_p = 2$. This is in line with the observation that the slipstream of the front propeller contracts (see Fig. 14) and thus at $d_y/R_p = 2$ the rear propeller does not experience the induced velocities in the slipstream of the front propeller. For any of the measurements with d_y smaller than 2, interaction effects can be expected. Because the front propeller slipstream increases the axial velocity inflow to a part of the rear propeller, the effective advance ratio of the rear propeller increases, and thus its C_T and C_P reduce, as can be deduced from Fig. 8. The more the propellers overlap, the more this effect on C_T and C_P is accentuated. However, the front propeller also introduces a swirl or tangential velocity component in the slipstream, and the effect of this induced velocity component on the rear propeller performance depends on the location of slipstream impingement. The sketch in Fig. 23 illustrates this effect. A tangential velocity component in the local propeller reference frame increases blade sections angle of attack when it opposes the direction of propeller rotation and vice versa. When the blade sections angle of attack increases, C_T and C_P increase as well. The tangential velocity component in the front propeller reference frame needs to be transformed to the rear propeller reference frame, which introduces a dependency on d_y. When reducing the lateral distance from $d_y/R_p = 2$ to $d_y/R_p = 1$, for corotating propellers, the rear propeller sees a relative increase in C_T and C_P by the tangential velocity component up to $d_y/R_p = 1$. Case 1 in Fig. 23 illustrates this opposing tangential

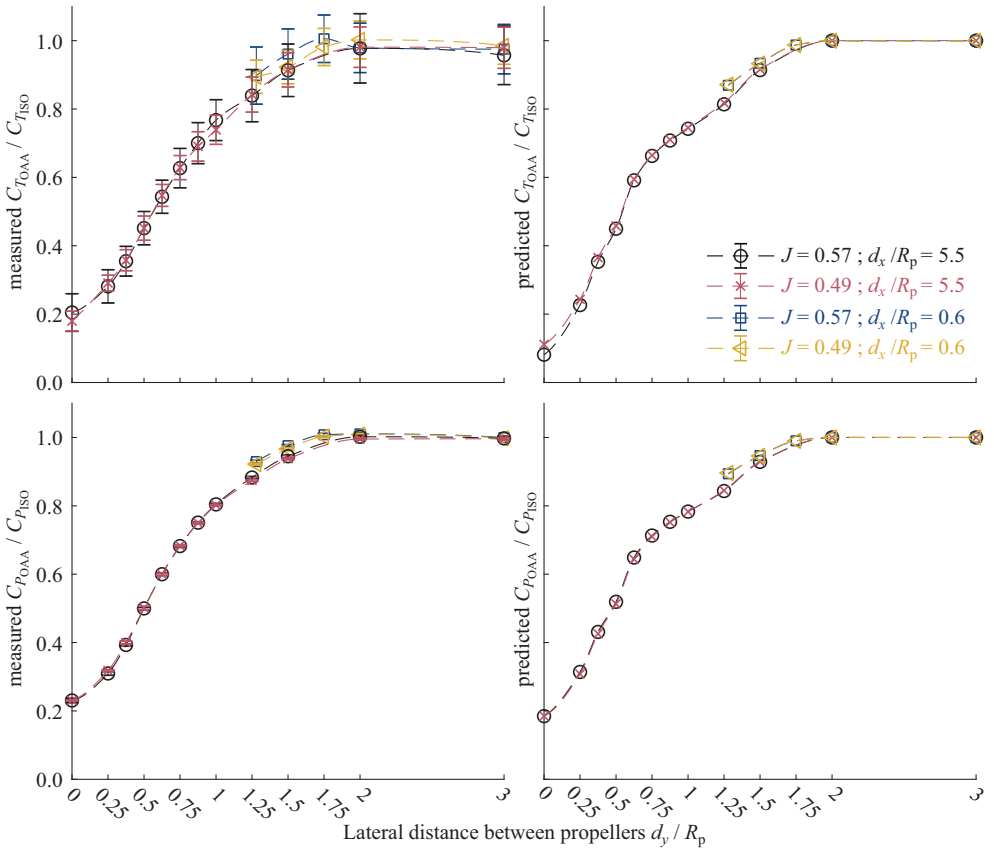

a) Measured with F/T sensor **b) Predicted with extended BEM model**

Fig. 22 Change of rear propeller C_T and C_P due to OAA interaction as function of d_y for $V_\infty = 20$ m/s and $\alpha_p = 0$ deg.

Downloaded by TU DELFT on August 19, 2021 | http://arc.aiaa.org | DOI: 10.2514/1.C035814

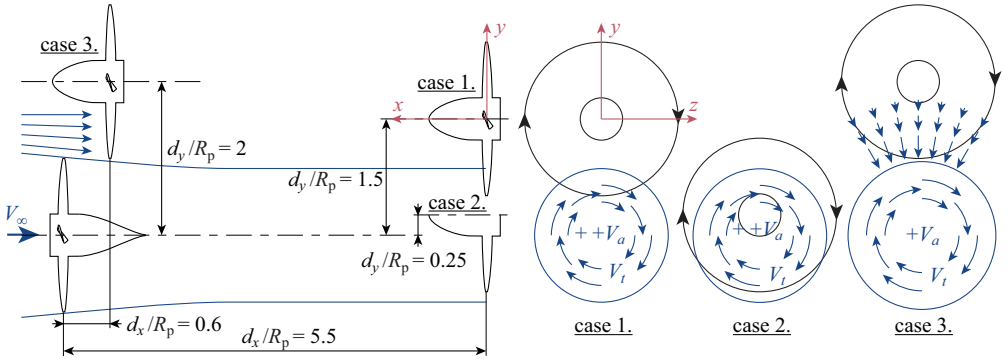

a) Top view of one-after-another interaction

b) Slip-stream impingement on rear propeller disk as seen from behind

Fig. 23 Sketch of the interaction of rear the propeller with slipstream of the front propeller in OAA configuration. Three cases of different axial and lateral distance are distinguished.

Downloaded by TU DELFT on August 19, 2021 | http://arc.aiaa.org | DOI: 10.2514/1.C035814

velocity to the rotation direction for $d_y/R_p = 1.5$. For $d_y/R_p < 1$, part of the propeller disk sees an increase and part of the disk a decrease of thrust and power by the tangential velocity component. When d_y becomes very small, for instance, for $d_y/R_p = 0.25$ as shown in case 2 in Fig. 23, the tangential velocity is mainly in the direction of propeller rotation, reducing thrust and power. At $d_y/R_p = 0$, the effect of the tangential velocity is purely reducing C_T and C_P. Hence, the largest impact on C_T and C_P can be expected for this condition. This effect of the tangential velocity can be clearly recognized in the measurements for $d_x/R_p = 5.5$ by the sudden change in slope around $d_y/R_p \approx 0.75$. The BEM model prediction features this slope change, too. The main deviation of the BEM model from the experimental result is found at $d_y/R_p = 0$. It is thought that, due to contraction of the slipstream, the area of the propeller disk affected by the slipstream does not increase anymore when reducing d_y at values slightly larger than $d_y/R_p = 0$. Therefore, a reduction in slope toward $d_y/R_p = 0$ would be expected and is also present in the experimental and BEM data. In the BEM data, this is less so, possibly due to a difference in slipstream contraction compared to the experiment. Note that, surprisingly, the relative interaction effects for both advance ratios are the same.

The results for $d_x/R_p = 0.6$ are slightly different. At $d_y/R_p = 2$, there is a slightly increased C_P of 1.0% due to interaction compared to the isolated propeller. Whether this is accompanied by a similarly increased C_T cannot be concluded due to the large confidence interval for this performance parameter; however, this is likely the case. At $d_y/R_p = 1.75$, still, a 0.5% increased C_P is found compared to the isolated propeller. For $d_y/R_p \leq 1.5$, C_T and C_P for the rear propeller decrease due to the interaction. The main difference for the close case compared to the far case is that the slipstream is less contracted (see Fig. 13), meaning that the axial velocity at the rear propeller plane induced by the front propeller is lower for the close case, but spread over a wider area. This reduces the effect of slipstream impingement on the rear propeller performance as the effective advance ratio is less increased. However, this does not explain directly any increase in C_P or C_T. A possible explanation is that when a propeller operates in the region of contraction of another propeller it experiences a local angle of attack, as sketched in case 3 for $d_y/R_p = 2$ in Fig. 23. From the results of Fig. 8, we know that operation at nonzero angle of attack increases C_T and C_P compared to the symmetric inflow case, thereby explaining the observation. At $d_y/R_p = 1.75$, when the front propeller slipstream already impinges on part of the rear propeller, the angle of attack effect apparently offsets the increased advance ratio effect. The BEM model does not capture this thrust increasing effect because the induced velocity components outside of the slipstream tube are zero in this model.

In Fig. 24, the corresponding in-plane force coefficients and out-of-plane moment coefficients of the rear propeller in OAA interaction are plotted. First, consider the data for $d_x/R_p = 5.5$. At $d_y/R_p = 3$, no in-plane forces or out-of-plane moments are present because the propeller operates outside the front propeller slipstream and does not experience any nonuniformities in its inflow. This is maintained at $d_y/R_p = 2$. Observe case 1 at $d_y/R_p = 1.5$ as sketched (in rear view) in Fig. 23. A decrease in thrust at the location of slipstream impingement results in a negative moment around the z axis, which is indeed reflected in the results shown in Fig. 24. Furthermore, the corresponding local reduction in the tangential force on the affected blade sections causes a negative C_{F_z}. Similarly to what happens at nonzero angle of attack, reductions in thrust and tangential force likely experience a phase lag, resulting also in a positive C_{M_y} and C_{F_y}. The generation of positive y moment and force is accentuated by the tangential velocity component, which relatively reduces thrust and tangential force more on the side of impingement with negative z coordinates. Around or slightly below $d_y/R_p = 1$, the effects for C_{F_z}, C_{M_y}, and C_{F_y} experience extrema, because the slipstream impingement results in the most imbalance of effect between the positive and negative sides of the propeller disk in the y direction. For C_{M_z}, this minimum is reached slightly later, probably because effects at the small y location do not weigh in as much as at the larger y location. The effects resulting in positive C_{M_y} and C_{F_y} and negative C_{M_z} are countered by effects on the positive side of the propeller disk in the y direction for $d_y/R_p < 1$, and therefore a decrease in magnitude toward $d_y/R_p = 0$ is seen for these components. For C_{F_z}, a different trend is seen. This force component changes sign and experiences a small maximum around $d_y/R_p = 0.25$. This may be caused by a phase shift in thrust and tangential force reduction, although this is not entirely clear from the available data. A surprising result is found for $d_y/R_p = 0$, where nonzero values of C_{M_y} and C_{F_y} were measured. In this axisymmetric condition in terms of inflow to the rear propeller, no in-plane forces and out-of-plane moments are expected. However, in Sec. IV.A, the effect of the fairing was discussed, and a local reduction in total pressure was found. A reduction in total pressure and thus a reduction in axial velocity locally results in a less decreased thrust of the rear propeller and may therefore have caused such an effect. As a result of the swirl, the exact location of this effect on the rear propeller is, however, not known, and therefore this explanation cannot be confirmed.

The interaction effects for $d_x/R_p = 0.6$ are very similar to the described effects for $d_x/R_p = 5.5$. The main difference is found in the C_{F_y} and C_{M_y} components. Already for $d_y/R_p = 3$, the rear propeller experiences a negative C_{F_y}, and this becomes more negative with a minimum at $d_y/R_p = 1.75$. C_{M_y} follows a similar pattern. The previously discussed angle of attack effect due to contraction of the slipstream, as sketched in case 3 in Fig. 23, would explain this difference in interaction compared to what was found for $d_x/R_p = 5.5$. The in-plane velocity components induced by the slipstream contraction cause a reduction in thrust and tangential force on the negative side of the propeller disk in the z direction compared to the positive side.

The question can be raised if the described interaction effects on the force and moment components are significant for aircraft stability.

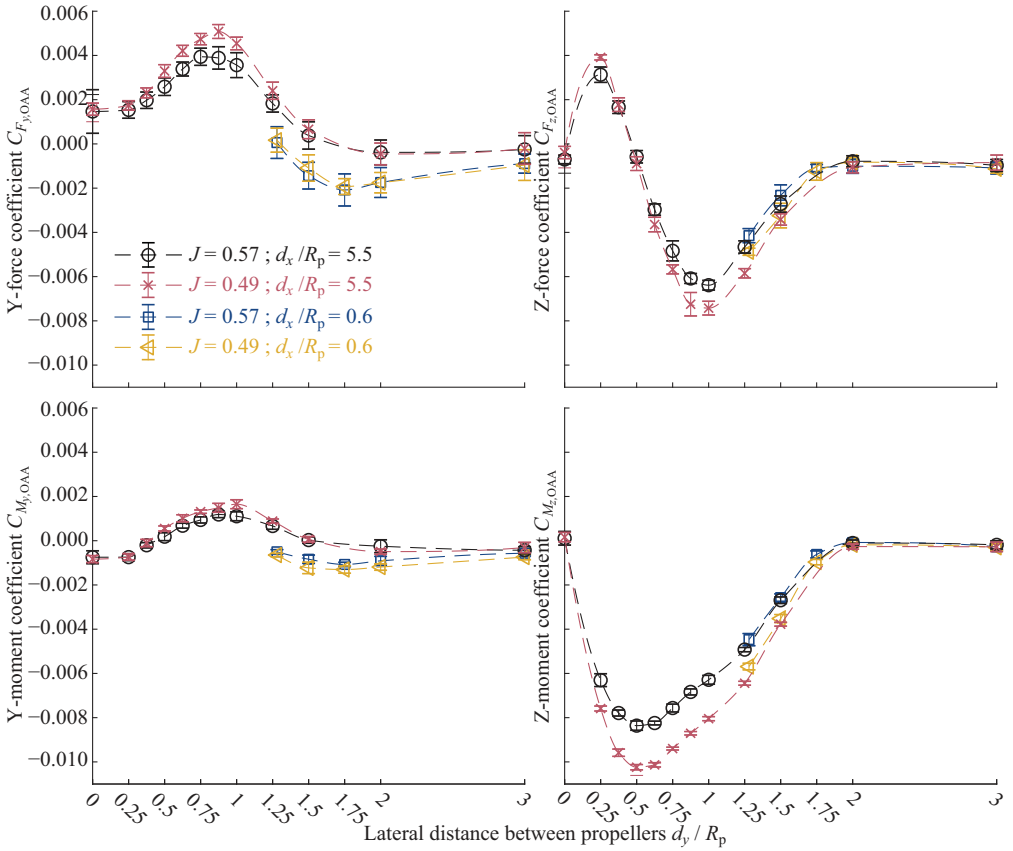

Fig. 24 Rear propeller in-plane force coefficients and out-of-plane moment coefficients due to OAA interaction as function of d_y for $V_\infty = 20$ m/s and $\alpha_p = 0$ deg.

Consider the layout of the Airbus Vahana as sketched in Fig. 1b. If the front propeller slipstreams impinge on the rear propellers when there is partial overlap, a pitchdown moment will be generated by the negative moment around the z axis and the positive force in the y direction. However, in terms of y force, this may be dependent on the rotation direction of the propellers. Because the rear propeller is mounted relatively high, the reduced thrust of the rear propeller could result in a pitch-up moment. The corresponding change of the rear propeller slipstream also impacts the loading on the horizontal and vertical tail planes. All in all, consideration of these interaction effects on aircraft stability seems important, nontrivial, and very layout dependent.

2. *Propellers at Equal Thrust*

Also, for the OAA configuration, the rear propeller rotational speed was varied to obtain the same T_C as without front propeller slipstream impingement. The result is given in Fig. 25 as the ratio of the power required for the rear propeller to the power of the isolated propeller to achieve the same T_C. Results are only shown for $d_x/R_p = 5.5$ because for $d_x/R_p = 0.6$ it cannot be assumed that the upstream effect on the front propeller thrust is negligible or small. Note that, because only the rear propeller power is considered and not the front propeller power, the power changes should be divided by 2 if compared to results for SBS interaction in Fig. 21. Results for two different advance ratios of the front propeller are shown, with measurements in Fig. 25a and BEM model predictions in Fig. 25b. Very significant power increases are found when the propeller overlap is large, increasing to values larger than 30% for full overlap at $d_y/R_p = 0$. The trends are again very similar for both advance ratios. Prediction with a BEM model of this interaction effect is clearly sufficiently accurate, and such a method could thus successfully be used for initial design purposes.

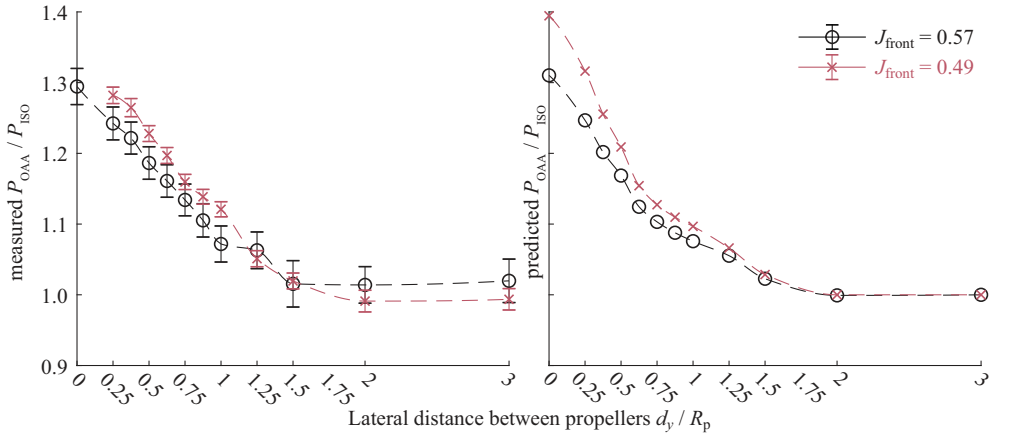

a) Measured with F/T sensor **b) Predicted with extended BEM model**

Fig. 25 Change of rear propeller power to maintain thrust in OAA interaction as function of d_y for $V_\infty = 20$ m/s and $\alpha_p = 0$ deg.

Downloaded by TU DELFT on August 19, 2021 | http://arc.aiaa.org | DOI: 10.2514/1.C035814

Downloaded by TU DELFT on August 19, 2021 | http://arc.aiaa.org | DOI: 10.2514/1.C035814

V. Conclusions

In this Paper, it is shown by means of experiment how propeller interaction in side-by-side and one-after-another configuration, as typically found on eVTOL vehicles, impacts propeller performance in terms of thrust, power, in-plane forces, and out-of-plane moments. The dependency of these results on relative propeller distances d_x and d_y is analyzed, too. For the one-after-another configuration, an extended blade element momentum model was used to predict the performance effects, which seemed to capture most interaction effects with sufficient accuracy.

For the side-by-side interaction case, interaction effects depend strongly on propeller angle of attack α_p and vary from weak interaction at small angles to strong interaction at larger angles. A large drop in rear propeller thrust and power of up to 30% was found for $\alpha_p = 90$ deg, depending strongly on advance ratio and lateral distance between the propellers d_y. With increasing lateral distance, the interaction effects become less pronounced. The dependency on the advance ratio was found to be different for the force and moment components. At large angle of attack, the rear propeller experiences a reduced effective angle of attack due to the downwash of the front propeller. The interaction effects for the front propeller were small to negligible and likely resulted from a small upwash from the rear propeller. The detrimental interaction results for the rear propeller may be indicative for eVTOL operation with such propeller configuration in the last stages of transition from vertical flight to forward flight. Compensation of the lost thrust in such a situation by increasing rotational speed of either the rear propeller or both front and rear propellers resulted in power penalties of 5 to 13% for the two propellers combined, again depending on the lateral distance.

The effects of interaction for the rear propeller in one-after-another configuration were also studied. For large axial distance d_x, when the front propeller slipstream is fully contracted, a maximum reduction of thrust and power of the rear propeller of up to 80% was observed for the configuration with full overlap. A dependency of the interaction on the swirl and thus rotation direction of the propellers was found. At small d_x, in the region of the front propeller slipstream contraction, a small increase in thrust for the rear propeller arose when the propeller was positioned outside of the front propeller slipstream, likely due to an induced angle of attack by the slipstream. This is the only thrust increasing interaction mechanism discovered in this research for any downstream-located propeller. Compensation of the lost thrust through a rotational speed increase of the rear propeller led to significant power penalties of up to 30% for the rear propeller alone. If this type of interaction occurs on an eVTOL vehicle like the Airbus Vahana, for instance, caused by a sudden change of angle of attack, the interaction effects experienced by the rear propeller may affect aircraft stability. This may not only happen through thrust reduction and its associated moments but also through generation of in-plane forces and out-of-plane moments.

The found interaction effects are demonstrative of propeller interaction on a wide range of eVTOL vehicles, but a strong dependency on the precise geometric layout as well as on the thrust level in case of the side-by-side configuration was found. Interaction of the propellers with static parts on such vehicles like wings may be of great importance, too. The results presented in this Paper can serve as a validated starting point for specific analyses with more realistic geometry.

Acknowledgments

The authors would like to thank Nando van Arnhem, Ph.D. candidate in the Flight Performance and Propulsion section, for the technical support during the wind-tunnel campaign. Furthermore, Peter den Dulk and Ed Roessen from the electronic and mechanical support division are acknowledged for manufacturing the test setup and problem solving during the wind-tunnel campaign.

References

[1] Brelje, B. J., and Martins, J. R. R. A., "Electric, Hybrid, and Turboelectric Fixed-Wing Aircraft: A Review of Concepts, Models, and Design Approaches," *Progress in Aerospace Sciences*, Vol. 104, Jan. 2019, pp. 1–19. https://doi.org/10.1016/j.paerosci.2018.06.004

[2] Anon., "*Aircraft Electrical Propulsion—The Next Chapter of Aviation?*" Roland Berger TR, Roland Berger Ltd., London, U.K., Sept. 2017.

[3] Anon., "Fast-Forwarding to a Future of On-Demand Urban Air Transportation," Uber, White Paper, Oct. 2016, https://www.uber.com/elevate.pdf.

[4] Johnson, W., Silva, C., and Solis, E., "Concept Vehicles for VTOL Air Taxi Operations," *AHS Technical Conference on Aeromechanics Design for Transformative Vertical Flight*, American Helicopter Society (AHS), 2018.

[5] Kim, H. D., Perry, A. T., and Ansell, P. J., "A Review of Distributed Electric Propulsion Concepts for Air Vehicle Technology," *2018 AIAA/IEEE Electric Aircraft Technologies Symposium*, AIAA Paper 2018-4998, 2018. https://doi.org/10.2514/6.2018-4998

[6] Kraenzler, M., Schmitt, M., and Stumpf, E., "Conceptual Design Study on Electrical Vertical Take Off and Landing Aircraft for Urban Air Mobility Applications," *AIAA Aviation 2019 Forum*, AIAA Paper 2019-3124, 2019. https://doi.org/10.2514/6.2019-3124

[7] Kasliwal, A., Furbush, N. J., Gawron, J. H., McBride, J. R., Wallington, T. J., Kleine, R. D. D., Kim, H. C., and Keoleian, G. A., "Role of Flying Cars in Sustainable Mobility," *Nature Communications*, Vol. 10, No. 1, 2019, pp. 1–9. https://doi.org/10.1038/s41467-019-09426-0

[8] Silva, C., Johnson, W. R., Solis, E., Patterson, M. D., and Antcliff, K. R., "VTOL Urban Air Mobility Concept Vehicles for Technology Development," *2018 Aviation Technology, Integration, and Operations Conference*, AIAA Paper 2018-3847, 2018. https://doi.org/10.2514/6.2018-3847

[9] Anon., "PAV—eVTOL Passenger Air Vehicle," 2019, https://www.aurora.aero/pav-evtol-passenger-air-vehicle/ [20 July 2019].

[10] Droandi, G., Syal, M., and Geoffrey, B., "Tiltwing Multi-Rotor Aerodynamic Modeling in Hover, Transition and Cruise Flight Conditions," *AHS International 74th Annual Forum & Technology Display*, American Helicopter Society (AHS), 2018.

[11] Ventura Diaz, P., Johnson, W., Ahmad, J., and Yoon, S., "The Side-by-Side Urban Air Taxi Concept," *AIAA Aviation 2019 Forum*, AIAA Paper 2019-2828, 2019. https://doi.org/10.2514/6.2019-2828

[12] Stoll, A. M., Bevirt, J., Pei, P. P., and Stilson, E. V., "Conceptual Design of the Joby S2 Electric VTOL PAV," *14th AIAA Aviation Technology, Integration, and Operations Conference*, AIAA Paper 2014-2407, 2014. https://doi.org/10.2514/6.2014-2407

[13] Borer, N. K., Patterson, M. D., Viken, J. K., Moore, M. D., Clarke, S., Redifer, M. E., Christie, R. J., Stoll, A. M., Dubois, A., Bevirt, J., Gibson, A. R., Foster, T. J., and Osterkamp, P. G., "Design and Performance of the NASA SCEPTOR Distributed Electric Propulsion Flight Demonstrator," *16th AIAA Aviation Technology, Integration, and Operations Conference*, AIAA Paper 2016-3920, 2016. https://doi.org/10.2514/6.2016-3920

[14] McLemore, H. C., and Cannon, M. D., "Aerodynamic Investigation of a Four-Blade Propeller Operating Through an Angle-of-Attack Range from 0 Deg to 180 Deg," NACA TN 3228, June 1954.

[15] Smith, H. R., "Engineering Models of Aircraft Propellers at Incidence," Ph.D. Thesis, Univ. of Glasgow, Glasgow, Scotland, U.K., 2015.

[16] Droandi, G., Gibertini, G., Grassi, D., Campanardi, G., and Liprino, C., "Proprotor–Wing Aerodynamic Interaction in the First Stages of Conversion from Helicopter to Aeroplane Mode," *Aerospace Science and Technology*, Vol. 58, Nov. 2016, pp. 116–133. https://doi.org/10.1016/j.ast.2016.08.013

[17] Sweet, G. E., "Hovering Measurements for Twin-Rotor Configurations with and Without Overlap," NASA TN D-534, 1960.

[18] Harris, F. D., "Technical Note: Twin Rotor Hover Performance," *Journal of the American Helicopter Society*, Vol. 44, No. 1, 1999, pp. 34–37. https://doi.org/10.4050/JAHS.44.34

[19] Ramasamy, M., "Measurements Comparing Hover Performance of Single, Coaxial, Tandem, and Tilt-Rotor Configurations," *AHS International Forum 69*, American Helicopter Society (AHS), 2013.

[20] Ramasamy, M., "Hover Performance Measurements Toward Understanding Aerodynamic Interference in Coaxial, Tandem, and Tilt Rotors," *Journal of the American Helicopter Society*, Vol. 60, No. 3, 2015, pp. 1–17. https://doi.org/10.4050/JAHS.60.032005

[21] Yoon, S., Lee, H. C., and Pulliam, T. H., "Computational Analysis of Multi-Rotor Flows," *54th AIAA Aerospace Sciences Meeting*, AIAA

Paper 2016-0812, 2016.
https://doi.org/10.2514/6.2016-0812
[22] Heyson, H. H., "Preliminary Results From Flow-Field Measurements Around Single and Tandem Rotors in the Langley Full-Scale Tunnel," NACA TN 3242, Nov. 1954.
[23] Dingeldein, R. C., "Wind-Tunnel Studies of the Performance of Multirotor Configurations," NACA TN 3236, Aug. 1954.
[24] Stepniewski, W. Z., and Keys, C. N., *Rotary-Wing Aerodynamics*, Dover, New York, 1984, pp. 182–210.
[25] Lee, J.-W., Oh, S.-J., Yee, K.-J., and Kim, D.-K., "Numerical Investigation on Overlap Effects of Tandem Rotors in Forward Flight," *International Journal of Aeronautical and Space Sciences*, Vol. 10, No. 2, 2009, pp. 63–76.
[26] Sheng, C., and Narramore, J. C., "Computational Simulation and Analysis of Bell Boeing Quad Tiltrotor Aero Interaction," *Journal of the American Helicopter Society*, Vol. 54, No. 4, 2009, Paper 42002.
https://doi.org/10.4050/JAHS.54.042002
[27] Otsuka, H., and Nagatani, K., "Thrust Loss Saving Design of Overlapping Rotor Arrangement on Small Multirotor Unmanned Aerial Vehicles," *2016 IEEE International Conference on Robotics and Automation (ICRA)*, 2016, pp. 3242–3248.
https://doi.org/10.1109/ICRA.2016.7487494
[28] Theys, B., Dimitriadis, G., Hendrick, P., and Schutter, J. D., "Influence of Propeller Configuration on Propulsion System Efficiency of Multi-Rotor Unmanned Aerial Vehicles," *2016 International Conference on Unmanned Aircraft Systems (ICUAS)*, 2016, pp. 195–201.
https://doi.org/10.1109/ICUAS.2016.7502520
[29] Brazinskas, M., Prior, S. D., and Scanlan, J. P., "An Empirical Study of Overlapping Rotor Interference for a Small Unmanned Aircraft Propulsion System," *Aerospace*, Vol. 3, No. 4, 2016, pp. 1–20.
https://doi.org/10.3390/aerospace3040032
[30] Nandakumar, G., Srinivasan, A., and Thondiyath, A., "Theoretical and Experimental Investigations on the Effect of Overlap and Offset on the Design of a Novel Quadrotor Configuration, VOOPS," *Journal of Intelligent & Robotic Systems*, Vol. 92, Nos. 3–4, 2018, pp. 615–628.
https://doi.org/10.1007/s10846-017-0707-2
[31] Zhou, W., Ning, Z., Li, H., and Hu, H., "An Experimental Investigation on Rotor-to-Rotor Interactions of Small UAV Propellers," *35th AIAA Applied Aerodynamics Conference*, AIAA Paper 2017-3744, 2017.
https://doi.org/10.2514/6.2017-3744
[32] Alvarez, E. J., and Ning, A., "High-Fidelity Modeling of Multirotor Aerodynamic Interactions for Aircraft Design," *AIAA Journal*, Vol. 58, No. 10, 2020, pp. 4385–4400.
https://doi.org/10.2514/1.J059178
[33] Ventura Diaz, P., and Yoon, S., "High-Fidelity Computational Aerodynamics of Multi-Rotor Unmanned Aerial Vehicles," *2018 AIAA Aerospace Sciences Meeting*, AIAA Paper 2018-1266, 2018.
https://doi.org/10.2514/6.2018-1266
[34] Bagai, A., and Leishman, J. G., "Free-Wake Analysis of Tandem, Tilt-Rotor and Coaxial Rotor Configurations," *Journal of the American Helicopter Society*, Vol. 41, No. 3, 1996, pp. 196–207.
https://doi.org/10.4050/JAHS.41.196
[35] Usai, D., "Aerodynamic Interaction Between Overlapping Propellers: A Numerical and Experimental Study," Master's Thesis, Polytechnic Univ. of Turin, Turin, Italy, July 2019.
[36] Veldhuis, L. L. M., Kotsonis, M., and van Berkel, E., "Non-Uniform Inflow Effects on Propeller Performance," *31st AIAA Applied Aerodynamics Conference*, AIAA Paper 2013-2801, 2013.
https://doi.org/10.2514/6.2013-2801
[37] Sinnige, T., and Veldhuis, L. L. M., "Pylon Trailing Edge Blowing Effects on the Performance and Noise Production of a Pusher Propeller," *52nd Aerospace Sciences Meeting*, AIAA Paper 2014-0566, 2014.
https://doi.org/10.2514/6.2014-0566
[38] Yang, Y., Sciacchitano, A., Veldhuis, L. L. M., and Eitelberg, G., "Analysis of Propeller-Induced Ground Vortices by Particle Image Velocimetry," *Journal of Visualization*, Vol. 21, No. 1, 2018, pp. 39–55.
https://doi.org/10.1007/s12650-017-0439-1
[39] Yeo, D., Atkins, E. M., Bernal, L. P., and Shyy, W., "Experimental Validation of an Aerodynamic Sensing Scheme for Post-Stall Aerodynamic Moment Characterization," *AIAA Atmospheric Flight Mechanics (AFM) Conference*, AIAA Paper 2013-4979, 2013.
https://doi.org/10.2514/6.2013-4979
[40] Gunasekaran, S., Altman, A., and Ol, M. V., "Errors in Off-Axis Loading of Off-the-Shelf 6-Component Force Transducers: A Cautionary Tale," *53rd AIAA Aerospace Sciences Meeting*, AIAA Paper 2015-1562, 2015.
https://doi.org/10.2514/6.2015-1562
[41] Verstraete, D., and MacNeill, R., "The Effects of Blockage on the Performance of Small Propellers," *20th Australasian Fluid Mechanics Conference*, 2016.
[42] Han, H., Xiang, C., Xu, B., and Yu, Y., "Experimental and Computational Analysis of Microscale Shrouded Coaxial Rotor in Hover," *2017 International Conference on Unmanned Aircraft Systems (ICUAS)*, 2017, pp. 1092–1100.
https://doi.org/10.1109/ICUAS.2017.7991413
[43] Heinzen, S. B., "Flight Testing of the Free-to-Pitch Variable Pitch Propeller," *2018 AIAA Aerospace Sciences Meeting*, AIAA Paper 2018-0762, 2018.
https://doi.org/10.2514/6.2018-0762
[44] Serrano, D., Ren, M., Qureshi, A. J., and Ghaemi, S., "Effect of Disk Angle-of-Attack on Aerodynamic Performance of Small Propellers," *Aerospace Science and Technology*, Vol. 92, Sept. 2019, pp. 901–914.
https://doi.org/10.1016/j.ast.2019.07.022
[45] Ortun, B., Boisard, R., and Gonzalez-Martino, I., "In-Plane Airloads of a Propeller with Inflow Angle: Prediction vs. Experiment," *30th AIAA Applied Aerodynamics Conference*, AIAA Paper 2012-2778, 2012.
https://doi.org/10.2514/6.2012-2778
[46] Stokkermans, T. C. A., and Veldhuis, L. L. M., "Propeller Performance at Large Angle of Attack Applicable to Compound Helicopters," *AIAA Journal*.
https://doi.org/10.2514/1.J059509
[47] Sayers, A. T., and Ball, D. R., "Blockage Corrections for Rectangular Flat Plates Mounted in an Open Jet Wind Tunnel," *Proceedings of the Institution of Mechanical Engineers, Part C: Journal of Mechanical Engineering Science*, Vol. 197, No. 4, 1983, pp. 259–263.
https://doi.org/10.1243/PIME_PROC_1983_197_107_02
[48] Langer, H.-J., Peterson, R. L., and Maier, T. H., "An Experimental Evaluation of Wind Tunnel Wall Correction Methods for Helicopter Performance," *AHS International Forum 52*, American Helicopter Society (AHS), 1996.
[49] Scarano, F., and Riethmuller, M. L., "Iterative Multigrid Approach in PIV Image Processing with Discrete Window Offset," *Experiments in Fluids*, Vol. 26, No. 6, 1999, pp. 513–523.
https://doi.org/10.1007/s003480050318
[50] Wieneke, B., "PIV Uncertainty Quantification from Correlation Statistics," *Measurement Science and Technology*, Vol. 26, No. 7, 2015, Paper 074002.
https://doi.org/10.1088/0957-0233/26/7/074002
[51] Glauert, H., "Airplane Propellers," *Aerodynamic Theory: A General Review of Progress*, edited by W. F. Durand, Vol. 4, Springer, Berlin, 1935, pp. 169–360.
[52] Snel, H., Houwink, R., and Bosschers, J., "Sectional Prediction of Lift Coefficients on Rotating Wind Turbine Blades in Stall," Netherlands Energy Research Foundation TR ECN-C–93-052, Petten, The Netherlands, Dec. 1994.
[53] Sears, W. R., "A Systematic Presentation of the Theory of Thin Airfoils in Non-Uniform Motion," Ph.D. Thesis, California Inst. of Technology, Pasadena, CA, 1938.
https://doi.org/10.7907/EM5X-CZ66
[54] Sears, W. R., "Some Aspects of Non-Stationary Airfoil Theory and Its Practical Application," *Journal of the Aeronautical Sciences*, Vol. 8, No. 3, 1941, pp. 104–108.
[55] Chandrasekaran, B., "Method for the Prediction of the Installation Aerodynamics of a Propfan at Subsonic Speeds," NASA CR 3887, Hampton, VA, 1985.
[56] Veldhuis, L. L. M., "Propeller Wing Aerodynamic Interference," Ph.D. Thesis, Delft Univ. of Technology, Delft, The Netherlands, June 2005.

Downloaded by TU DELFT on August 19, 2021 | http://arc.aiaa.org | DOI: 10.2514/1.C035814

This article has been cited by:

1. Reynard de Vries, Nando van Arnhem, Tomas Sinnige, Roelof Vos, Leo L.M. Veldhuis. 2021. Aerodynamic interaction between propellers of a distributed-propulsion system in forward flight. *Aerospace Science and Technology* **118**, 107009. [Crossref]

Downloaded by TU DELFT on August 19, 2021 | http://arc.aiaa.org | DOI: 10.2514/1.C035814